A STUDY OF EFFICIENCY DROOP OF GREEN LIGHT EMITTING DIODES GROWN BY METALORGANIC CHEMICAL VAPOR DEPOSITION

A Master Thesis

Presented to

The Academic Faculty

By

Nordine Sebkhi

In Partial Fulfillment

Of the Requirement for the Degree

Master of Science in the School of Electrical and Computer Engineering

Georgia Institute of Technology

December, 2011

A STUDY OF EFFICIENCY DROOP OF GREEN LIGHT EMITTING DIODES GROWN BY METALORGANIC CHEMICAL VAPOR DEPOSITION

Approved by:

Dr. Russell Dupuis, Advisor
School of Electrical and Computer Engineering
Georgia Institute of Technology

Dr. Shyh-Chiang Shen
School of Electrical and Computer Engineering
Georgia Institute of Technology

Dr. Paul Douglas Yoder
School of Electrical and Computer Engineering
Georgia Institute of Technology

Date Approved:

ACKNOWLEDGEMENTS

I would like to begin by thanking everyone who made my work possible and enriching. First of all, I am grateful to my advisor, Dr. Russell Dupuis, for giving me the priceless opportunity to work at the Advanced Materials and Devices Group. In addition to his support and help, he has provided me with his expertise on MOCVD and LEDs to thrive and gain an invaluable experience.

Also, I would like to thank Dr. Jae-Hyun Ryou for the opportunity to have worked on interesting and meaningful projects, and for his support. Then, I would like to express my thanks to my colleagues, Jeomoh Kim, Mi-Hee Ji and Zachary Lochner with whom I worked closer and have shared unforgettable memories as good friends. It is these colleagues who are responsible for the success of this group, and who have shown me what hard work is.

Finally, my gratitude is also extended to our collaborating professors, Dr. Shyh-Chiang Shen and Dr. Douglas Yoder, to kindly serve as thesis committee members. They are taking on their invaluable time to review this thesis.

TABLE OF CONTENTS

LIST OF FIGURES

SUMMARY

The objective of this thesis is to discuss the solutions investigated by AMDG (Advanced Materials and Devices Group) to reduce the "efficiency droop" effect that occurs in III-Nitrides Light Emitting Diodes (LEDs) when driven at high injection current densities. The efficiency droop refers to a decrease of the LED light emission efficiency when increases the current density from low values ~10A/cm^2 to higher values >100A/cm^2. Many scientific papers have been written about the possible reasons for this phenomenon. Therefore, this thesis will discuss the different effects suspected to contribute to the droop, and discuss LED structure modifications studied by Dr. Dupuis' research group to reduce their impact. In addition to a description of a conventional LED structure, a discussion of the device fabrication process will be provided including the solutions investigated in our group to improve LED performance.

Because measurement is critical to our studies, a description of the equipment used by the AMDG will be provided, e.g., the Electroluminescence (EL) and Photoluminescence (PL) test stations, Atomic Force Microscopy (AFM) for surface topology, TLM for metallic contact resistivity, X-Ray diffraction for crystal quality and epitaxial layer structure, and Hall-Effect measurement for doping concentration characterization and material resistivity.

Because the IQE gives us a direct assessment of the active region's crystal quality, the setup and operation of a new Temperature-Dependent PL (TD-PL) system to measure the Internal Quantum Efficiency (IQE) was the main focus of this research. The External Quantum Efficiency (EQE) is measured using electroluminescence measurements. The

EL measurements involve the acquisition of the emitted light spectrum along with different processed data such as the Full-Width at Half Maximum (FWHM) of the spectral intensity, the peak wavelength, output power, etc., which allows a comparison of the different LED structure performances.

Within this work, a new LabVIEW© program (called QuickTest 2.0) has been developed in order to automate the instrumentation setup and improve both the speed and accuracy of EL acquisition.

A brief description of the G language used by the LabVIEW© software will be provided along with the objective and motivation for upgrading the program, the general features of the program, and a comparison of spectrum acquisition and processed data results. The benefit for the research in the AMDG was to reduce measurement time, improve efficiency, supply a more user-friendly front-panel, and to enable transfer to other computers.

INTRODUCTION

1.1. Why is the LED a new promising technology

The principle of light emission exists in many different forms, e.g., incandescence, fluorescence, gas discharge luminescence, or solid state lighting (SSL) using Light-Emitting Diodes (LEDs). Introduced as a practical electronic component in 1962, early LEDs emitted only red light, but modern versions are available with emission across the visible, ultraviolet and infrared wavelengths.

When a light-emitting diode is forward biased, electrons are able to recombine with holes within the device, releasing energy in the form of photons. This effect is called electroluminescence and the color of the light (corresponding to the energy of the photon) is determined by the energy gap of the semiconductor. LEDs are often small in area (less than 1 mm^2), and integrated optical components may be used to shape its radiation pattern. LEDs present many advantages over other light sources including lower energy consumption, longer lifetime, improved robustness, smaller size, faster switching, and greater durability and reliability.

Light-emitting diodes are used in applications as diverse as automotive lighting, traffic signals, full-color outdoor displays, and background lighting in handheld electronic devices. Their high switching rates are also useful in advanced communications technology as optical emitters for emerging fiber optic networks. Infrared LEDs are also used in the remote control units of many commercial products. Currently, LEDs are being

developed for general lighting applications where their particular characteristics such as efficiency, longevity, durability, compactness and cool operation are needed. The worldwide lighting market will grow to approximately $159 billion in 2020, with 80% of that total from general lighting, according to a report from McKinsey & Company (LEDs magazine, “Lighting market report predicts strong growth for LED lighting”, September 2011). However, to be able to lead the technological revolution in the general lighting market, LEDs need to cover the full visible spectrum in order to emit true white color. So far, red and blue LEDs are well mastered, but when one approaches green wavelengths, their efficiency decreases. This is the so-called “green gap” due to the internal quantum efficiency reduction as the LED active region design incorporates more In into the active region. Efficiency droop affects virtually all III-N LEDs but is much more pronounced as the wavelength gets longer. However it is still a significant effect even for blue LEDs.

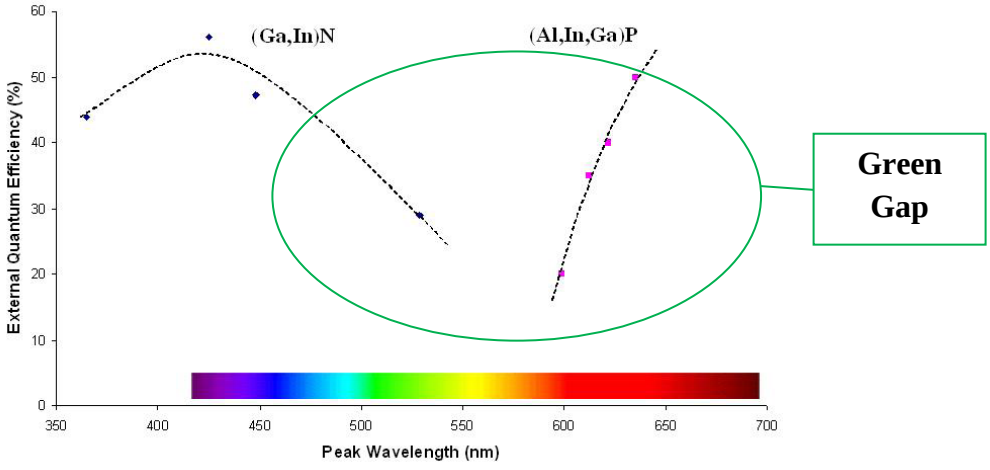

Figure 1.1: External Quantum Efficiency for the visible spectrum [1]

Therefore, the challenge we are facing today is to fabricate green LEDs that can emit light as bright as blue and red ones to obtain white color based on the RGB (Red Green Blue) combination. The major difference between red and blue/green LEDs is that the former is made of InAlGaP grown on GaAs and the latter of InGaN grown on GaN.

1.2. Overview of AMDG

AMDG stands for Advanced Materials and Devices Group, and is under the direction of Dr. Russell Dupuis and the supervision of Dr. Jae-Hyun Ryou. So far, the group possesses two cleanrooms. The first one is composed of three Metalorganic Chemical Vapor Deposition (MOCVD) reactors, one dedicated for GaAs-related material growth and the other two for GaN-related materials. The second cleanroom is dedicated to device testing and material characterization. A list of equipment will be described in the Chapter 4. An optics lab is also used for photoluminescence measurements. The current main focus of the group is to grow III-Nitride devices such as blue/green LEDs, UV Laser Diode (LD) structures, along with HFETs and HBTs.

The crystal growth is performed in the group's cleanroom, while device measurement and characterization mostly in our device testing lab, and the device fabrication process is performed in the Microelectronics Research Center (MiRC) as well as the Nanotechnology Research Center (Marcus Center).

2. CRYSTAL GROWTH BASICS

2.1. III-Nitride Materials

2.1.1. Generalities, direct and indirect bandgaps

III-Nitrides are a group of binary, ternary, and quaternary compound crystals formed by atoms of the group III in the Periodic Table (3 valence electrons) and Nitrogen in group V (5 valence electrons). Their major characteristics are large bandgap energies (compared to GaAs for example), high thermal stability and a direct bandgap which makes them ideal for optoelectronic applications.

In a direct bandgap semiconductor, an electron in the conduction band can fall directly to an empty state in the valence band, giving off the energy difference as a photon of light. In an indirect bandgap semiconductor, an electron in the conduction band must undergo a momentum change as well as changing its energy (for example through a defect state) before falling to the valence band. The energy is usually given up as heat to the lattice rather than as an emitted photon. Therefore, a crystal with a direct bandgap can be used to create brighter LEDs while minimizing generation of heat. The following figure illustrates the difference between direct and indirect bandgap.

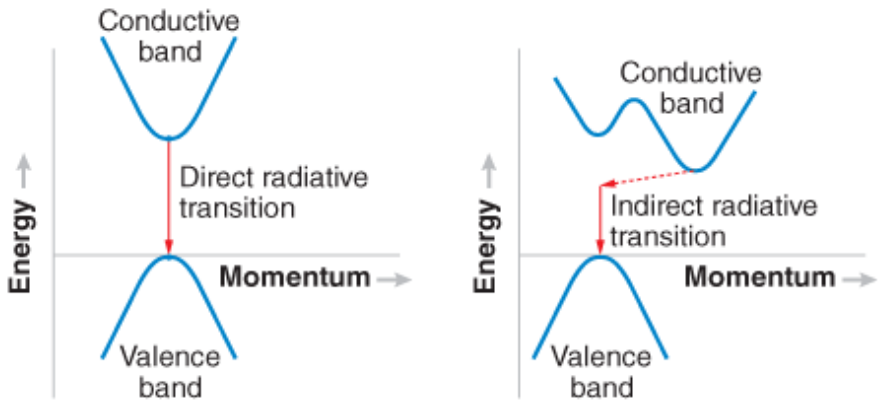

Figure 2.1: (left) direct vs (right) indirect bandgap [2]

The bandgap energy (ΔE) is directly linked to the wavelength of emission (λ) through the following equation:

$$\Delta E = \frac{h.c}{\lambda} \qquad (2.1)$$

Where h is the Planck constant and c is the speed of the light in free space.

The III-Nitride alloys that are of interest in this thesis are GaN, InGaN, AlGaN and InAlN. A GaN crystal has a larger bandgap energy (3.4 eV) compared to GaAs (1.43 ev), which corresponds to UV wavelengths. However, when indium (In) or aluminum (Al) is added to GaN, the bandgap energy can be engineered to allow photon emission in the visible spectrum depending on the composition of each additional element in the GaN-based alloy (In or Al). Refer to the following figure for the spectrum range that InGaN, AlGaN and AlInN cover.

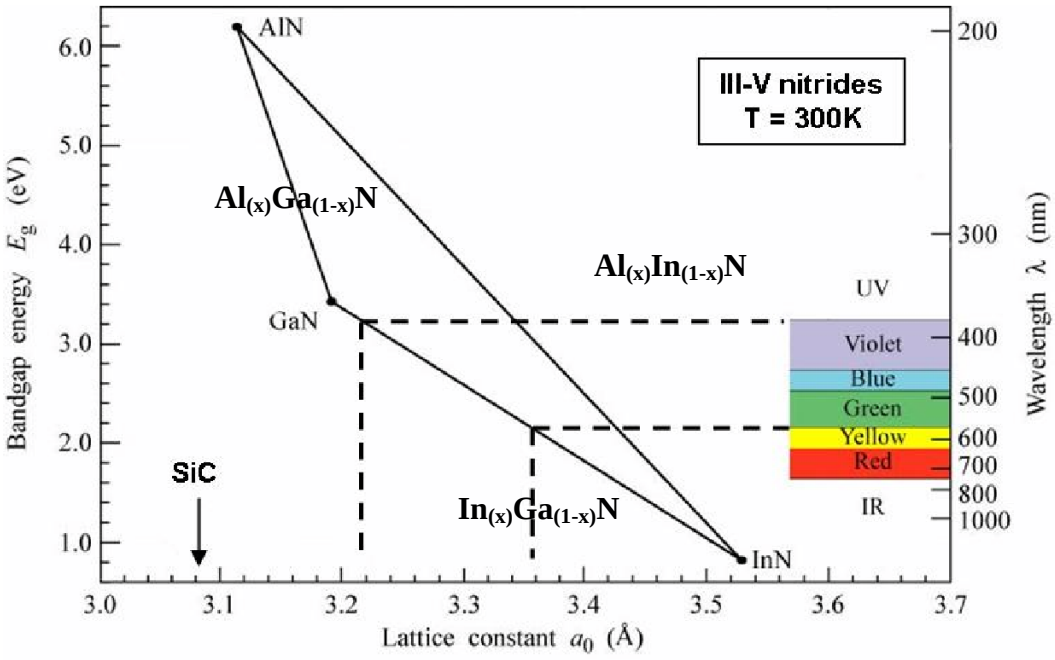

Figure 2.2: Spectrum of emission in function of In, Al and Ga concentrations in III-Nitrides alloys [3]

The bandgap energy (E_g in eV) can be determined based on the composition (x in percentage) of each element in the alloys using the Vegard's law:

$$\mathrm{E_{g_{In(x)Ga(1-x)N}}}(\mathrm{x}) = \mathrm{x}.\mathrm{E_{g_{In}}} + (1-\mathrm{x}).\mathrm{Eg_{.GaN}} + \mathrm{b}.\mathrm{x}.(1-\mathrm{x}) \qquad (2.2)$$

$$\mathrm{a_{In(x)Ga(1-x)N}}(\mathrm{x}) = \mathrm{x}.\mathrm{a_{InN}} + (1-\mathrm{x}).\mathrm{a_{GaN}} + \mathrm{b}.\mathrm{x}.(1-\mathrm{x}) \qquad (2.3)$$

The variable a (in Å) is the lattice constant of the crystal. The parameter b (in eV) is called bowing parameter. In practice, the curves are not linear like in the Figure 2.2 but are bowed. The bowing parameter is determined experimentally according to the crystal quality and the alloy composition. The following figure shows the impact of different values of the bowing parameter. In general, the bowing parameter is set at around 1 eV.

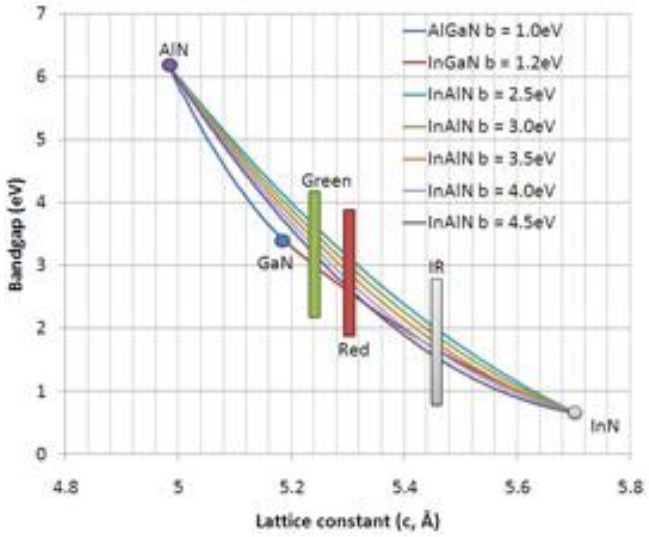

Figure 2.3: InAlN and InGaN Bandgaps with different bowing parameters [4]

2.1.2. Hexagonal Wurtzite crystals

The wurtzite crystal structure consists of two interpenetrating hexagonal close-packed sub-lattices. Each sub-lattice is shifted along the c-axis by 3/8 of the cell height. GaN, AlN, or InN exhibits a stable hexagonal wurtzite crystal structure rather than a meta-stable zincblende structure.

In an ideal wurtzite structure, the c/a ratio is 1.633. The deviation from the ideal c/a ratio increases as the electronegativity difference between group III atoms and group V atoms increases. The *c/a* ratio can also be correlated with the differences in electronegativity. AlN has *c/a*=1.601 and GaN exhibits a *c/a*=1.627 while InN shows *c/a*=1.612. The difference is attributed to the creation of the dipole, resulting in polarization. The unit cell of the wurtzite crystal structure is shown in the following figure.

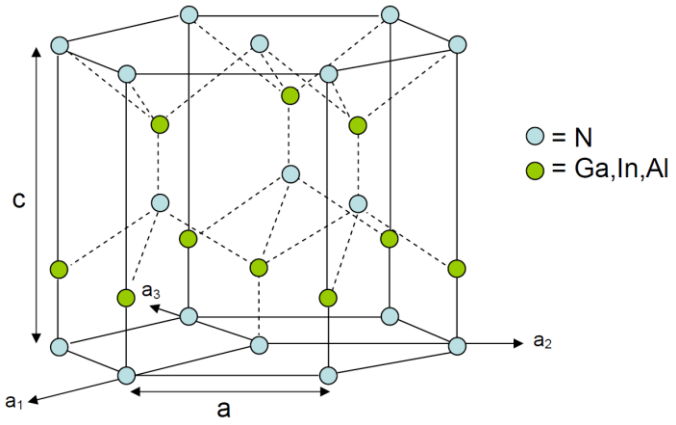

Figure 2.4: Wurtzite unit cell [5]

The major issue to overcome with the group III-Nitrides is lack of a large-area, high-quality lattice-matched substrate. Indeed, it is of prime importance to have an excellent crystal quality in order to increase device lifetime and efficiency by limiting or even avoiding dislocations due to lattice mismatch between the substrate and layers above. Obviously, a GaN substrate allows a better lattice matching for visible LEDs, which reduces the polarization effect due to the strain-free interface. However, the fabrication of "free-standing" GaN-substrate wafers is complex (typically, vapor-phase transport or epitaxial-type growth is used), and only a small number of companies produce them, leading to a cost-prohibitive price (several thousand dollars for a 2'' wafer) for the mass production of LED devices. Among other substrates, the most commonly and widely used is (0001) sapphire due to its hexagonal symmetry, thermal stability, availability and low cost. However, the major drawback is a large lattice mismatch with (0001) GaN, around 13%, which results in crystal strain and defect formation in epitaxially grown layers.

2.1.3. Doping of GaN

Intrinsically, GaN is an n-type semiconductor. However, because of a relatively low background carrier concentration (10^{15} to 10^{16} cm^{-3}), GaN is doped in order to increase the free carrier concentration. Silicon and germanium are the two main n-type dopants but silicon is more generally used because the limit of the free-carrier concentration is larger with Si-doping (4×10^{18} cm^{-3}) due to relatively low ionization energy of Si donors (about 20 meV) compared to Ge-doping.

P-type doping in III-N materials is one of the major technical challenges to overcome in order to improve LED device performance. Magnesium (Mg) is generally used as a dopant in GaN based materials for p-type layers. But Mg-doped GaN epitaxial layers do not have a high electrical conductivity, because of hydrogen bonding for example, and the doping efficiency is only around 1% due to a large ionization energy of Mg (around 120 meV). However, a more "active region friendly" layer can be grown with InGaN:Mg because p-InGaN layer is grown at lower temperature to avoid indium in the active region to be ejected out and the Mg acceptor activation energy is lower in InGaN:Mg than for GaN:Mg (see section 3.4).

2.2. Metalorganic Chemical Vapor Deposition

Metalorganic chemical vapor deposition (MOCVD) has been developed over the past forty years to become the dominant epitaxial materials technology for both research and production for III-Nitride-related materials growth. This technique has enabled LEDs to become commercially viable. The MOCVD epitaxial growth technology was pioneered

in 1968 by Manasevit, et al. [6] by demonstrating the heteroepitaxial growth of III-V materials on insulating substrates. But, because of the early stage of its development, the epitaxial layers suffered from impurity related defects. In 1977, Dupuis et al. [7, 8] have demonstrated the first practical devices with AlGaAs/GaAs solar cells and quantum well injection lasers.

The fundamental principle of the MOCVD is to introduce two or more materials in a gaseous form into a reaction chamber where they chemically react with one another to form a new material deposited on the wafer surface. The MOCVD growth technique involves a sequence of chemical reactions among different precursors. A metalorganic precursor exists in either liquid or solid form and is stored in an all-welded stainless steel container, commonly referred to as "bubbler". A carrier gas passes (or bubbles) through the precursor container and carries metalorganic precursor molecules into an epitaxial growth chamber; thus, precursors must exhibit an appropriate volatility. Also, precursors should have the proper reactivity to thermally decompose in an epitaxial growth chamber. Trimethylgallium (TMGa), triethylgallium (TEGa), trimethylaluminum (TMAl), and trimethylindium (TMIn) are commonly used as group III precursors. Concerning the group V sources (Nitrides), the use of ammonia (NH_3) is the most common. The general reaction to form group III-Nitrides is described below.

$$R_3M + NH_3 \leftrightarrow MN + 3 \cdot RH \qquad (2.4)$$

In this equation, R is an alkyl group, for instance methyl (CH_3) or ethyl (C_2H_5) and M represents the group III metal such as gallium (Ga), aluminum (Al), or indium (In).

N represents the group V elements such as P, As, N, or Sb, and H is hydrogen. In the case of GaN, trimethylgallium (TMGa) and ammonia (NH_3) react based on the following equation.

$$(CH_3)_3Ga + NH_3 \leftrightarrow GaN + 3 \cdot CH_4 \qquad (2.5)$$

The MOCVD growth process can be categorized into four processes: gas input, pyrolysis, diffusion, and surface reaction. Then, a by-products formed during the epitaxial growth, such as C_2H_6, are pumped away with carrier gases. Figure 2.5 shows the schematic illustration of GaN epitaxial growth. The MOCVD system used in our group is equipped with Close-Coupled Showerhead (CCS) growth technology. CCS technology can provide inherently growth uniformity due to precursor diffusion governed by mass transport from completely and uniformly intermixed gas phases. Metalorganic group III precursors are introduced into the top plenum chamber and hydride precursors are introduced into the lower plenum chamber through a water-cooled showerhead surface over the entire area of deposition. The showerhead is constructed to enable precursors to be separated right up to the point where they are injected onto the substrates via high density of injection nozzles. The complete intermixed uniform distribution of gas phases is created at approximately 5 mm out of total 11 mm spacing between the showerhead and a substrate. The linear vertical temperature distribution in a growth chamber with CCS configuration can lead to high uniformity precursor decomposition efficiency. In addition, close packed wafer configuration results in high area utilization. These two factors produce high precursor utilization efficiency.

The three-zone heater system creates the temperature uniformity via modification of the temperature profile, resulting in higher yield.

The figure 2.6 illustrates the basic diagram of an MOCVD.

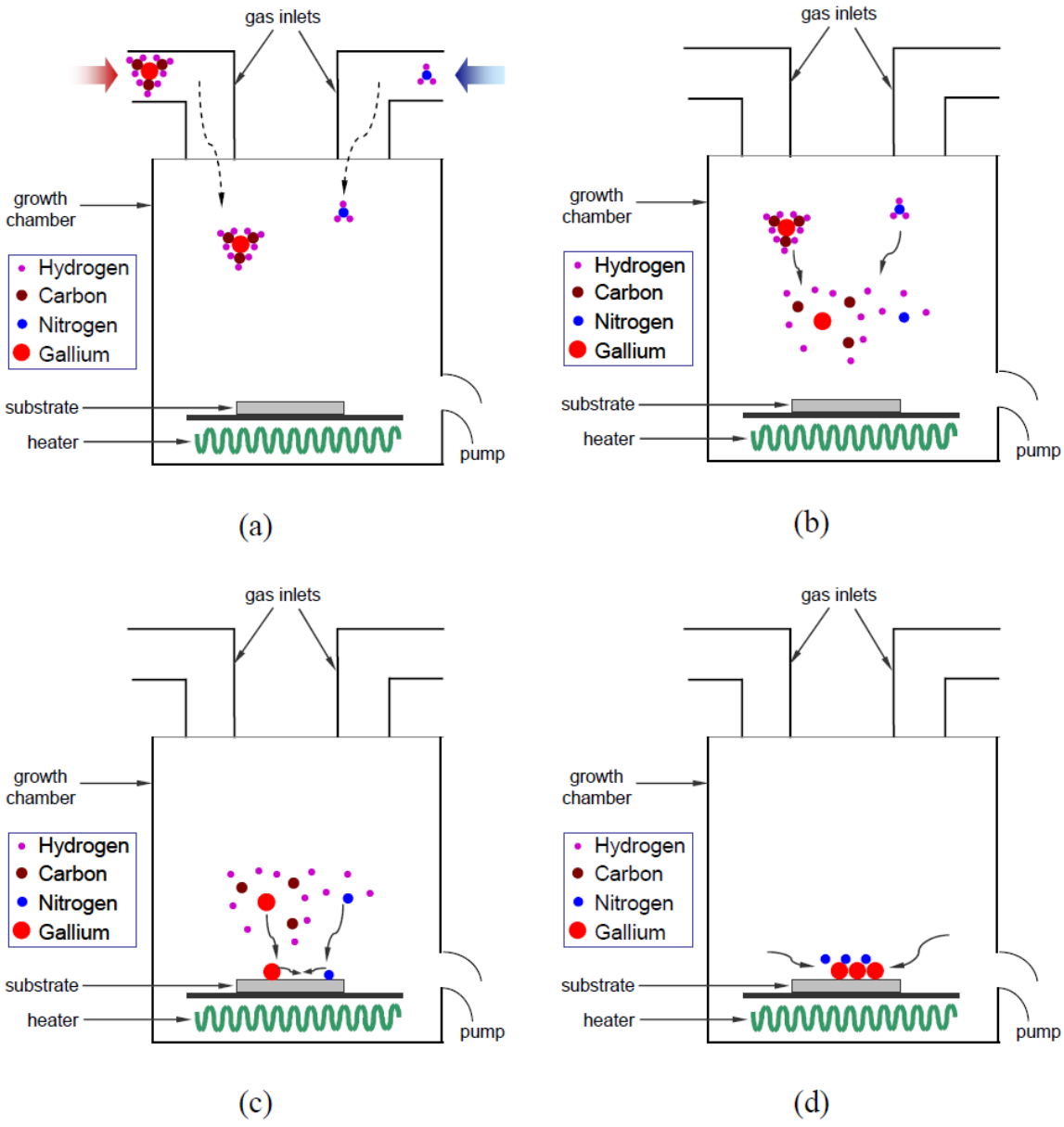

Figure 2.5: Illustration of MOCVD epitaxial growth process (a) gas input (b) pyrolysis (c) diffusion and (d) surface reaction [9]

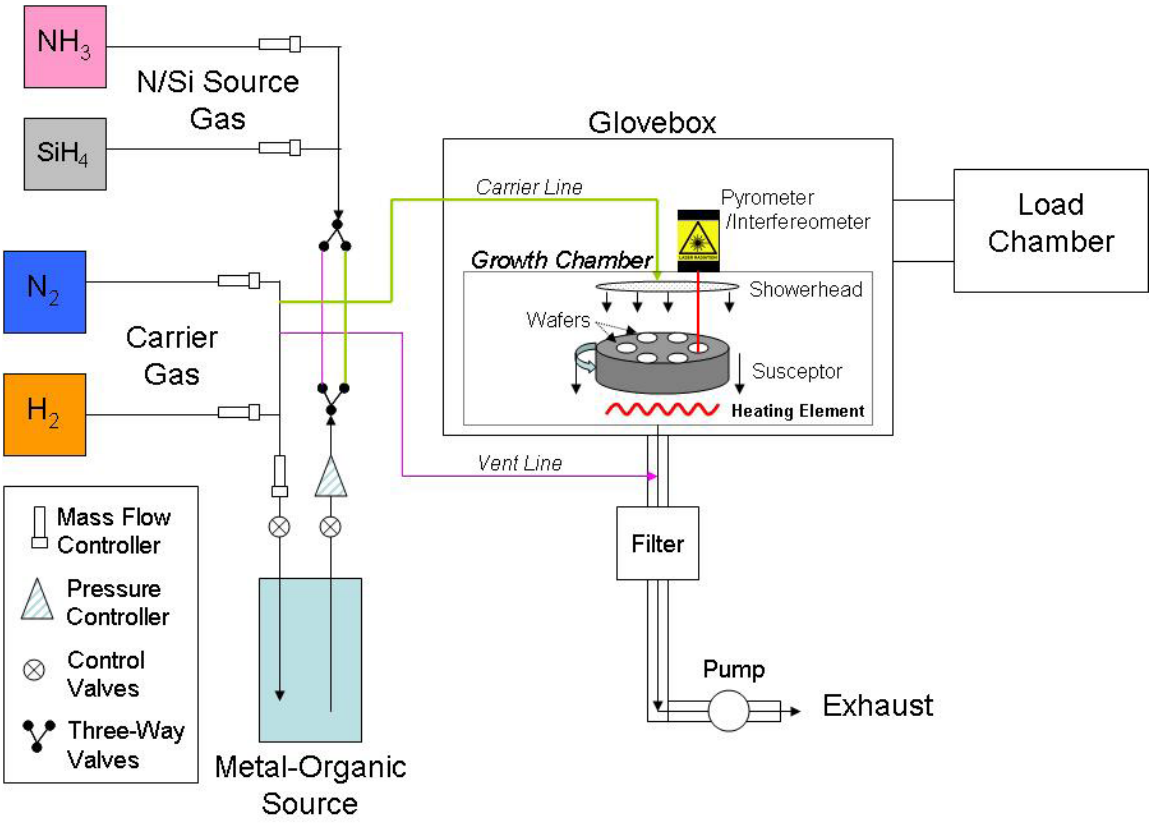

Figure 2.6: Basic diagram of an MOCVD reactor [5]

3. LED DEVICE BASICS

3.1. Principle

Light-Emitting Diodes are a special type of a p-n junction. A current is injected in the device where electrons flow from the n-type layer to the p-type, and inversely for holes. Then electrons and holes recombine in the "active region" of the LED located between the n-type and p-type layers. Because of de-excitation of electrons in the conduction band when recombined with holes in the valence band, photons are emitted at a wavelength function of the bandgap energy.

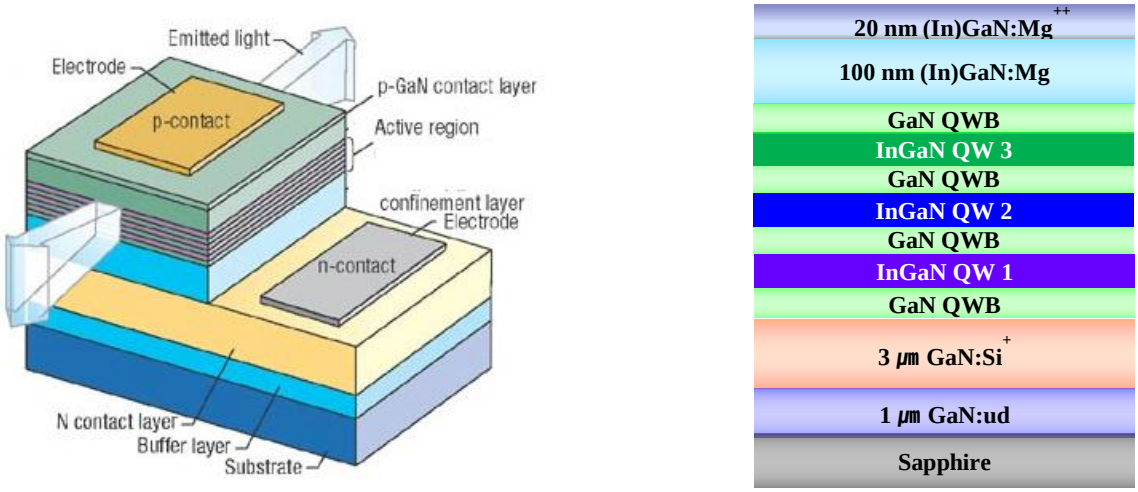

Figure 3.1: (Left) Conventional Structure [10] and (Right) Triple-Quantum Well Structure

The following sub-sections will discuss the principal layers of an LED structure. But at first, we will begin with a general overview of the characteristics of a p-n junction.

3.2. P-N junction

A p-n junction is composed of one region uniformly p-doped in one side and one n-doped on the other side.

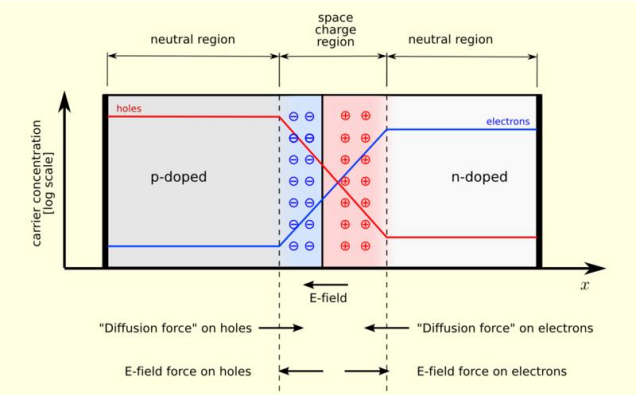

Figure 3.2: Illustration of a p-n junction [11]

When the two regions are put into contact, a diffusion of carriers occurs because the n-material has a large concentration of electrons and conversely for the p-material. A diffusion current is then established from n-side to p-side for electrons and inversely for the holes. The resulting diffusion current cannot build up indefinitely because an opposing electric field is created at the junction as electrons leave behind uncompensated donor ions (N_d^+) in the n-side, and holes leaving uncompensated acceptors (N_a^-). This electric field is in the direction opposite to that diffusion current for each type of carrier. Therefore, the field creates a drift component of the current, opposing the diffusion

current. The result is a net current equals to zero at the equilibrium as well as a built-in voltage V_0.

When the p-n junction is forward-biased, the potential barrier that exists at the space charge region is lowered due to an opposite applied electric field compared to the built-in field. The consequence is the flow of carriers is facilitated because of a low potential barrier. A current induced by the flow of the majority carriers is then created.

3.3. N-Type Layer

The n-type layer of a GaN-based LED structure is usually composed of GaN doped with silicon. The choice of using silicon donors comes from the small ionization energy of donor-bound electrons. A small ionization energy means that silicon donors can easily give off electrons to the conduction band, resulting in a higher concentration of free electrons. Free-electron concentrations can be controllably changed from 10^{17} to $2x10^{19}$ cm^{-3} by varying the flow rate of silane (SiH_4), the precursor used for Si doping of GaN in MOCVD. Si substitutes for a Ga atom in the lattice and provides a loosely bound electron. The ionization energy is on average 22 meV. In the AMDG MOCVD systems, the optimal flow rate of silane during GaN:Si growth is 12 sccm, and the resistivity of the resulting GaN:Si epitaxial layer is ~0.004 Ohm-cm.

The growth of the n-type GaN layer is nowadays well mastered and produces a good crystal quality.

3.4. P-Type Layer

As previously indicated, the p-type layer is currently one of the most critical issues in the improvement of LED performance. Magnesium (Mg) is the most commonly used p-type dopant in GaN based materials grown by MOCVD, using bis-cyclopentadienyl magnesium (Cp_2Mg) as precursor. But, Mg has a tendency to bond with atomic hydrogen (derived from the pyrolysis of NH_3 during growth) in the crystal, which makes the Mg acceptors inactive as a dopant in this case. Some methods have been developed in order to break these hydrogen bonds, such as Low Energy Electron Beam Irradiation (LEEBI) or thermal annealing. But even then, the doping efficiency is quite low (1%) because of the large ionization energy of Mg acceptor states (around 120 meV). The resistivity of GaN:Mg in our LED structure is ~1.6 Ohm-cm which is around 300 times higher than n-type layer (~0.004 Ohm-cm). Therefore, a loss of injected holes occurs as they recombine nonradiatively and thus dissipate the energy as heat rather than contributing to the radiative recombination in the active region.

P-type InGaN is one of the most promising materials because it is grown under conditions which are more "active region friendly" than *p*-type GaN. InGaN is grown at a lower temperature than GaN which prevents damage to the InGaN quantum wells in the active region. Indeed, a high temperature growth can be responsible for indium to be ejected out from the crystalline structure of the active region, resulting in crystal quality degradation. Besides, the Mg acceptor activation energy is lower for InGaN:Mg than for GaN:Mg, which permits to obtain higher free-hole concentration at 300K, above 10^{18} cm^{-3}. Furthermore, using InGaN p-type layer may reduce the contact resistance due to a smaller bandgap energy [12].

However, the drawback is a higher lattice-mismatch because the last layer in the active region is GaN, which results in increasing polarization effect.

A typical thickness of our p-type layer in the LED structure is around 120 nm.

3.5. Active Region

The active region is the core of the LED structure and this region in the LED determines the way that the photons created by electron-hole radiative recombination are emitted. Two types of active region are typically employed: single quantum well (SQW) and multiple quantum well (MQW).

In our structure, the MQW is composed of two different III-N materials, usually GaN as the quantum-well barrier and InGaN as the quantum well in which radiative recombination occurs.

The thickness of the whole active region is around 60 nm (one quantum barrier + one quantum well is equal to approximately 15 nm). Depending on the indium composition of the alloy, the bandgap energy can be engineered to target the desired wavelength of emission. MQW structures enhance the confinement of carriers in multiple thin regions where injected carriers can recombine at a higher rate than for a SQW because of higher carrier densities inside wells (wells in MQW structures are thinner than for SQWs).

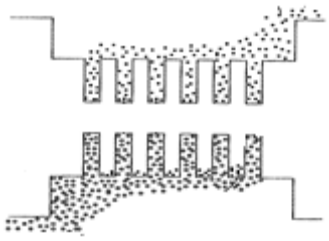

Figure 3.3: Illustration of a MQW structure [13]

But, increasing the carrier density enhances nonradiative recombination such as Auger recombination which leads to a degradation of performance.

Furthermore, because of a difference of effective masses between holes and electrons, the recombination occurs mainly close to the p-type layer instead of having a uniform distribution over the SQW, or trapped in all QWs in the MQW structure.

3.6. Electron Blocking Layer

Because the effective mass of electrons is seven times lighter than holes, electrons have a tendency to propagate faster. Therefore, some electrons recombine in the p-type layer or reach the metallic contact leading to a leakage current. This undesirable current flow is referred as a current overflow or carrier "spillover" (see section 3.8.2).

One way to tackle this issue is to incorporate an electron-blocking layer (EBL) that reduces the flow of electrons through the p-type layer by creating a high potential barrier between active region and p-type layer. The thickness of the EBL is typically between 5 to 20 nm.

The EBL is usually made of AlGaN because it has a larger energy bandgap than the GaN barriers and InGaN wells in the active region. However, better performance has been experienced using InAlN rather than AlGaN. The reasons and results are discussed in section 3.9.

Another way of improving the electron-blocking mechanism may be to use a graded electron-blocking layer (GEBL). A research group in Taiwan from National Chiao-Tung University has developed a GEBL that reduces efficiency droop compared to devices with a conventional AlGaN EBL [14]. The efficiency droop for the GEBL LED at an injection current density of 200 A/cm^2 is only 4% from the peak value, compared to 34% with a conventional single EBL. The following figure shows that the originality of this approach is a dissymmetry about its effect on the energy bands. The conduction band quantum barrier is increased, which reduces electron propagation, while the barrier in the valence band is decreased which may improve hole propagation.

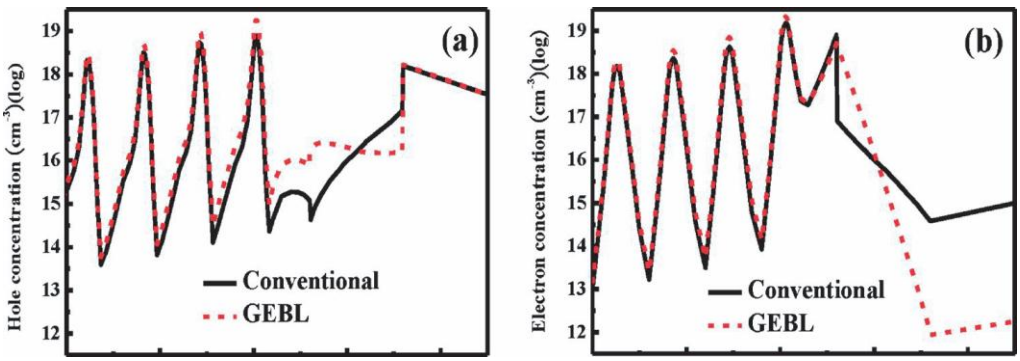

Figure 3.4: (a) hole and (b) electron concentrations distribution of conventional and GEBL LEDs at a current density of 100 A/cm^2 [14]

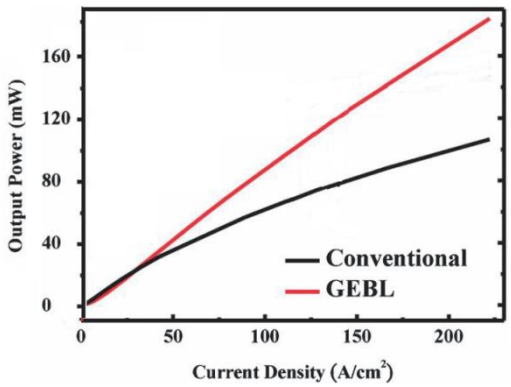

Figure 3.5: Output power function of current density for conventional and GEBL LEDs (adapted from [14])

3.7. Device Fabrication

The device fabrication is done after the growth of the entire LED structure. It is composed of four steps: Mesa etching, N-contact deposition, P-spreading metal deposition and P-bonding pad deposition.

Mesa etching (1): Mesa etching is a technique used to pattern the LED wafer structure in order to create regions for placing the ohmic contacts to the n-type and p-type layers. The first step is a photolithography: spreading a photoresist (PR) coating over the sample surface, alignment of the mask and PR exposure to UV light, PR development, deposition of SiO_2, and finally PR removing. Then, dry etching is done by Inductively Coupled Plasma (ICP) technique in our cleanroom.

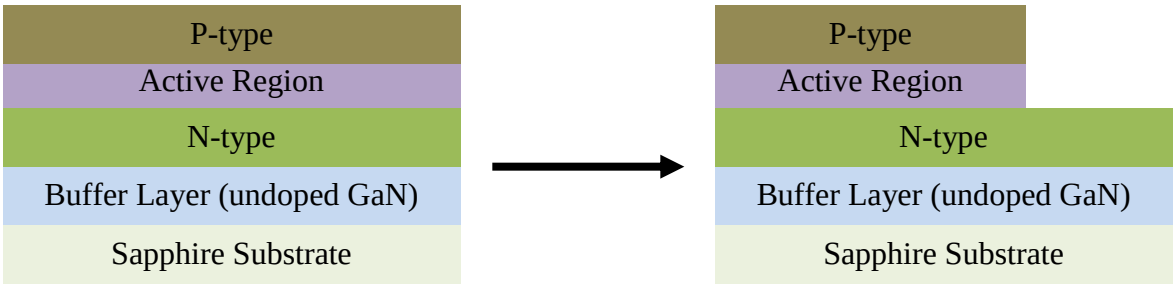

Figure 3.6: Illustration of the mesa-etching (not in scale)

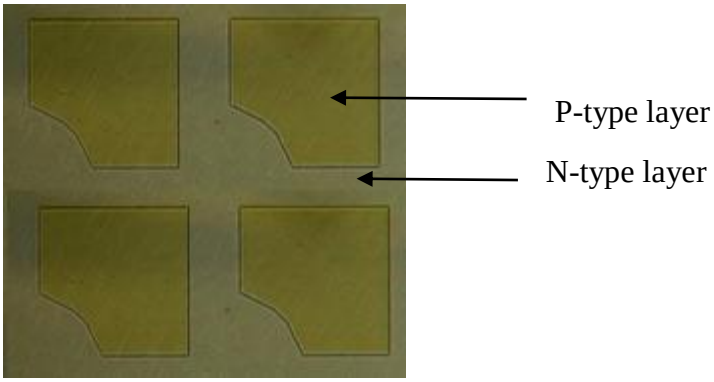

Figure 3.7: Image of the sample surface after mesa-etching (Courtesy of AMDG)

N-contact metal deposition (2): The second step is to deposit a metallic contact on the n-type layer using an e-beam evaporator. An E-beam evaporator is a physical vapor deposition system that heats up a metal in the solid state by bombarding the target with a highly energetic electron beam produced by a charged tungsten filament under high vacuum. The electron beam causes a region in the target metal source to melt and atoms from the target to transform into a gaseous phase. Then, these atoms travel through the vacuum and precipitate into solid form, coating the sample surface with a thin layer of metal. The metal used for n-contact is a superposition of different layers of metal:

Titanium (221 Å) / Aluminum (905 Å) / Titanium (269 Å) / Gold (460 Å). Then, a rapid thermal annealing (RTA) is carried out in order to improve the contact quality at a temperature of 700 ^{o}C.

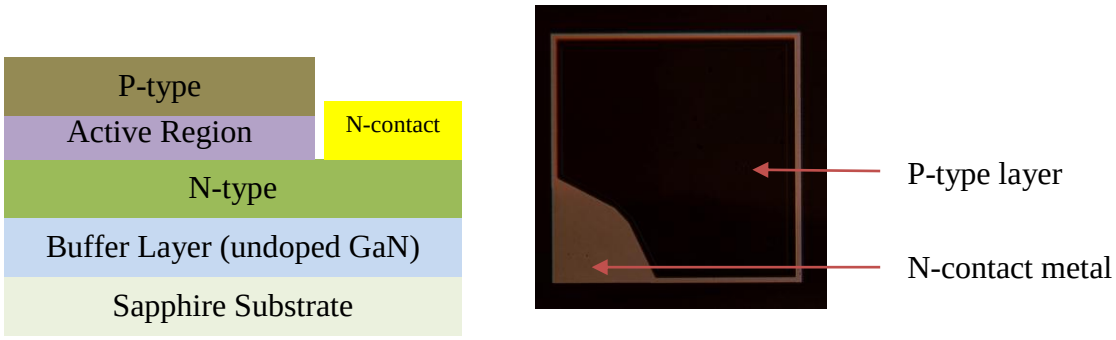

Figure 3.8: (Left) Schematic and (Right) image after n-contact metal deposition (Courtesy of AMDG)

P-spreading metal deposition (3): The third step is the deposition of a current spreading layer on top of the p-type layer. The use of a current spreading layer is crucial because it permits a better distribution of holes over the p-type layer. The process uses photolithography and the deposition of Nickel (60 Å) / Gold (60 Å) layers if transparent metal is desired or Nickel / Silver for a reflective contact, using e-beam evaporator. Then, an RTA process is carried out at 500 ^{o}C.

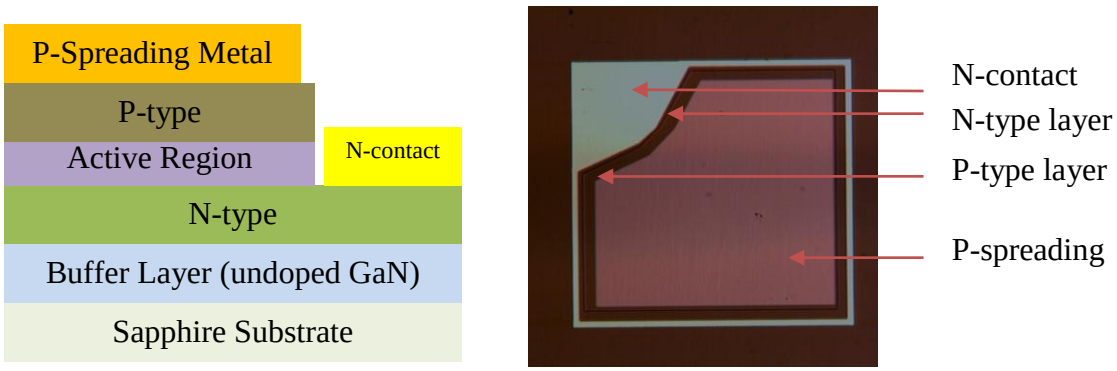

Figure 3.9: (Left) Schematic and (Right) image after p-spreading metal deposition (courtesy of AMDG)

P-bonding pad deposition (4): This is the last step of the device fabrication process. As stated previously, the p-type layer suffers from poor hole transport due to difficulties in growing highly conducting *p*-type III-N layers. Therefore, improving the ohmic contact quality is of prime importance to increase holes injection into the p-type layer. One of the solutions is to add a layer of gold (around 200 nm) in top of the p-spreading contact layer for bonding purpose. We have to note that the gold bonding layer is not transparent to the visible wavelengths.

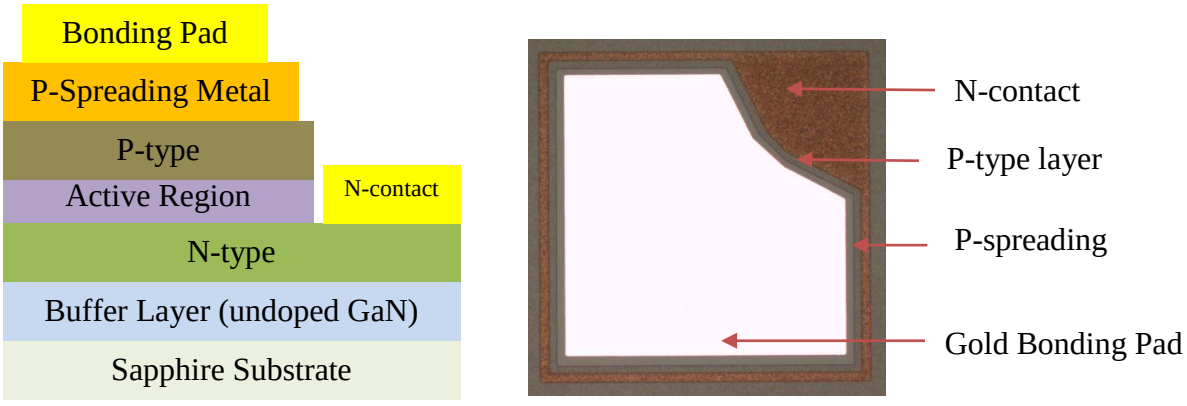

Figure 3.10: (Left) Schematic and (Right) image after p-bonding pad deposition (courtesy of AMDG)

3.8. Efficiency Droop

LEDs require an electrical current to be injected into the structure in order to emit light. The general trend is the higher the injected current is, the brighter the emitted light is. But, for GaN-based LEDs, beyond a certain current density (approximately 10 A/cm^2), this trend tends to degrade with increasing injection current, which has been referred to "efficiency droop". The causes of this phenomenon are still not well understood. The following figure illustrates the efficiency droop in the EL of blue LEDs grown with different p-type layers but emitting at the same wavelengths. The normalized integrated intensity (plotted on the Y-axis) is the result of the integration of the EL intensity over a wavelength range (usually from 350 nm to 700 nm for blue and green LEDs) and then normalized according to the highest integrated intensity's value.

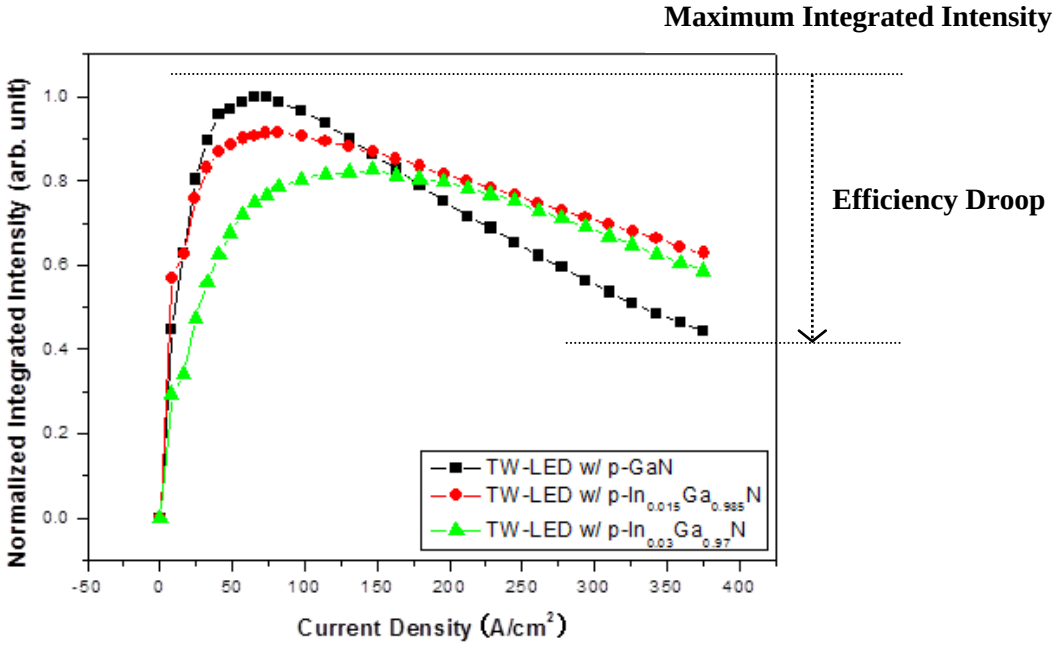

Figure 3.11: Illustration of the Efficiency Droop (AMDG Internal Document)

Many different contributions to droop have been identified, explained and discussed in the literature: current overflow [15], poor carrier injection efficiency [16][17][18], polarization fields [19][20], Auger recombination [21], junction heating [22], carrier delocalization from quantum dots [23], exciton dissociation [24], high plasma carrier temperature [25] and quantum-confined Stark effect [26]. Among these nonradiative recombination, Auger effects, current overflow (or current spillover), and polarization effects represent perhaps the main mechanisms responsible for the observed efficiency degradation. However, at this time, no one can undoubtedly state which one dominates. Various experiments have been developed in order to observe the impact of one effect over the others. To illustrate this controversy [27], researchers from Philips Lumileds are among those that believe Auger recombination is the source of the efficiency droop effect [28], while others from Virginia Commonwealth University criticize this idea and argue the difference in effective mass between electrons and holes is mainly responsible for the efficiency fall-off [29].

In a different route [20], Rensselaer Polytechnic Institute's researchers are convinced that the polarization effect in the Quantum Well (QW) enhances the leakage of injected electrons into the p-type layer, which, according to them, is the primary mechanism that leads to an efficiency droop.

The aim of this thesis is to describe different ideas that the AMDG group is investigating to reduce the efficiency droop by improving LED structures. The studies carried out in our group are focused on the reduction of the current overflow effect by using an optimized electron-blocking layer, increasing hole injection and transport efficiencies by

optimizing the p-InGaN layer and the InGaN MQW active region, and polarization effect by engineering the crystal growth of the multiple quantum wells on the active region.

The following sub-chapters will introduce the most important contributors to the efficiency droop that are currently under intense investigation: Auger recombination, current overflow and polarization effects.

3.8.1. Auger Recombination

Auger recombination is a nonradiative mechanism in which the electron-hole recombination is dissipated by the excitation of a free electron high into the conduction band, or by a hole deeply excited into the valence band. The highly excited carriers will subsequently lose energy by multiple phonon emission until they are close to band edge. The Auger recombination rate can be expressed as [30]:

$$U_{Auger} = C_n \, x \, \Delta n \, x \, (n_0 + \Delta n)^2 \qquad (3.1)$$

where C_n represents the Auger recombination coefficient for electrons, n_0 the equilibrium and Δn the excess carrier concentrations.

An increased current in an LED leads to an increased carrier concentration in the active region, so one expects that Auger recombination will become an important loss factor at some stage due to its dependence to the third power of the carrier density.

At high current injection densities, the Auger recombination rate can be expressed by the following equation.

$$\text{For } \Delta n >> n_0 : \; U_{Auger} \approx C_n \, x \, \Delta n^3 \qquad (3.2)$$

As it is dependent to the third power of the carrier density, this can lead to a possible main source for the efficiency droop in our LEDs because the multiple quantum well structures that we mostly use confine the carriers in a small volume which results in higher carrier densities compared to conventional double heterostructure active regions.

However, Auger recombination is greater for relatively small bandgap materials compared to large bandgap semiconductors such as GaN. In fact, the Auger recombination carrier lifetime is given by a modified expression of Beattie and Landsberg [31]:

$$\tau = \left[\frac{E_g\,(T)}{kT}\right]^{3/2} e^{\left[\frac{1+2M}{1+M}\frac{E_g(T)}{kT}\right]} \qquad (3.3)$$

Where k is the Boltzmann constant, T the temperature, $E_g\ (T)$ temperature dependent energy bandgap, and M the electron to hole mass ration.

The carrier lifetime expresses the average time during which the effect is occurring. A small carrier lifetime means that the effect should be predominant as it is occurring at a faster pace, which means that more carriers are impacted by this effect, compared to higher lifetime ones where the occurrence is slower.

As we can see from the equation (3.3), the Auger recombination carrier lifetime is dependent upon the value of the energy gap. Therefore, a large bandgap energy such as GaN (around 3.4 eV) has a higher Auger carrier lifetime compared to GaAs (about 1.4 eV), but the quantum efficiency of GaAs LEDs are quite good, which tends to discredit this effect. Furthermore, theoretical studies have found values of the Auger recombination coefficient for GaN devices which are too small to account for the experimental results [32].

However, Auger recombination is actually divided in two mechanisms: direct and indirect. The following figure illustrates the difference between direct and indirect Auger recombination.

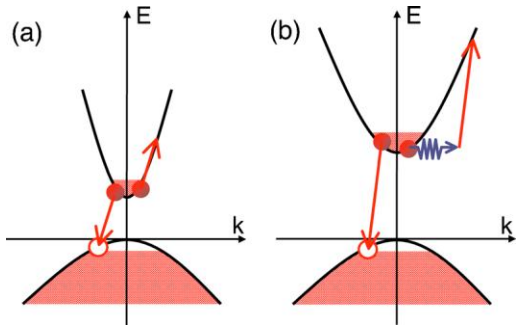

Figure 3.12: Illustration of (a) direct and (b) indirect Auger recombination [33]

The previous discussion was about the direct Auger recombination mechanism. The indirect Auger recombination (IAR) is mediated by a scattering mechanism, which provides additional momentum and enables Auger transitions to connect to a broader range of final states. This process is important in the nitrides and can account for at least some of the efficiency droop effects in nitride LEDs [33].

One scattering mechanism that assists IAR is the electron–phonon interaction, which is particularly strong in the nitrides [34]. Another scattering channel is introduced in the active region, made of InGaN layers, by the alloy-induced symmetry reduction. Charged defects may also scatter carriers and cause Auger recombination. Phonon- and alloy-assisted Auger processes are strong and cumulatively account for a sizeable Auger coefficient [33].

Thus, the indirect Auger recombination is currently one of the first candidates as a contributor to efficiency droop due to theoretical and experimental results [33] that show a high value for the indirect Auger recombination coefficient.

3.8.2. Current Overflow

Current overflow is a carrier loss mechanism in which electrons recombine outside the active region either radiatively (in which case the recombination occurs at an undesired wavelength) or nonradiatively, or collected by the metallic contact. The reason is that electrons have an effective mass seven times lighter than holes in GaN-related materials, which allows them to propagate faster in the crystal. Therefore, when a current is applied to the LED structure, the injected electrons reach the opposite extremity of the active region while a smaller quantity of injected holes have the time to penetrate into the active region, resulting in an significant number of electrons in the conduction band that can’t recombine. Therefore, these electrons propagate further and penetrate in the p-type layer or even collected in the metallic contact, referred to an overflow (or spillover) effect.

One important field of research is to find a way to increase the mobility of holes in the p-type layer and active region in order to enhance the electron-hole

radiative recombination. One example of structure modification comes from workers at Virginia Commonwealth University who have proposed [29] to reduce the thickness of the barrier in an InGaN multiple quantum well structure, from 12 nm to 3 nm, allowing better hole penetration. They claimed to have increased the current density of the peak external quantum efficiency from 200 A/cm^2 to 1100 A/cm^2. Another idea under investigation in our group is to optimize the electron blocking layer (refer to section 3.9.3) between the active region and the p-type layer that acts as a barrier to electron propagation. Therefore, much more electrons are retained in the active region, thus enhancing radiative recombination.

Recently, a graded electron-blocking layer (GEBL) has been introduced [14] to overcome some issues due to a single layer EBL.

3.8.3. Polarization effects

Polarization effects are composed of two components, piezoelectricity and spontaneous polarization. Piezoelectricity is produced by mechanical strain in the crystal, the polarization being proportional to the strain and changing sign with it. This is also known as the direct piezoelectric effect; the converse effect is when a crystal is strained when an electric field is applied. In the case of GaN-based LEDs, the direct effect induces a built-in potential because of the strain between different materials due to lattice parameter differences which implies a distortion of the electronic band structure and leads to a spatial separation of the electron and hole wave functions inside the QWs.

Therefore, electrons and holes are separated towards opposite sides of the layer, resulting in a reduction in the energy of confined electron-hole pairs and a reduced wave function overlap. This is referred as the Quantum-Confined Stark Effect (QCSE) [26]. The following figure illustrates the band diagram bending in the case of a QCSE.

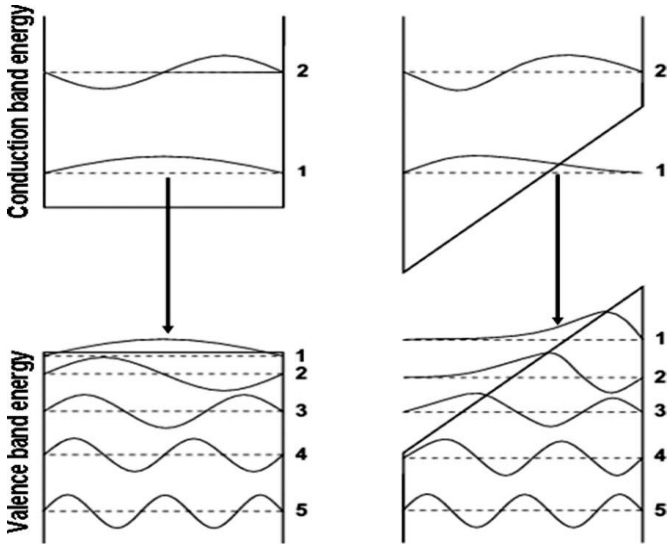

*Figure 3.13: Spatial separation of electron and hole wave functions in QCSE [*26*]*

3.9. Improvement of LEDs

3.9.1. Hole Transport

The study of hole transport is focused on the transport of the holes into the active region when using InGaN instead of GaN p-type layer in our LED structure. A p-GaN layer is commonly grown in blue LEDs because of a better lattice-match with the GaN quantum barrier which is typically used in this case. Even if the GaN:Mg layer is grown at high temperature, the damage on the indium in InGaN quantum wells for blue LEDs is

not strong enough to degrade the overall performance [35]. But, when it comes to green wavelengths, the growth temperature of the p-type layer greatly impacts the quality of the active region due to a high indium composition of the quantum wells, leading to low quantum efficiency. Therefore, the idea is to use InGaN p-type layer in order to lower the growth temperature, referred as "active region friendly" layer.

Thus, the objective of this research is to determine the difference of light emission efficiency between using p-GaN or p-InGaN with different In compositions. To keep track of hole propagation in the active region, a Triple-Wavelength MQW has been fabricated and is composed of three quantum wells of different indium compositions in order to emit at three different wavelengths (10% for 425 nm, 17% for 460 nm, and 23% for 520 nm). EL measurement is used to monitor hole propagation in the active region by showing emitted wavelengths.

So far, there is no clear evidence of improvement, but points out interesting problems that are still not explained. In the following figure, a Triple-Wavelength MQW structure was fabricated with a p-GaN layer (left) and p-InGaN layer (right). The EL spectrum of the structure with a p-InGaN layer shows an emission of three peak wavelengths, thus demonstrating the propagation of holes through the three quantum wells. Therefore, an improvement of hole transport may be experienced. But, when compared to the sample with a p-GaN layer, the conclusion can't be clearly extracted from the results. The EL spectrum shows the emission of two distinct peak wavelengths, but they correspond to the first and third quantum wells, which raise questions about what has happened in the second quantum well that explains a quasi-inexistent light emission from that well.

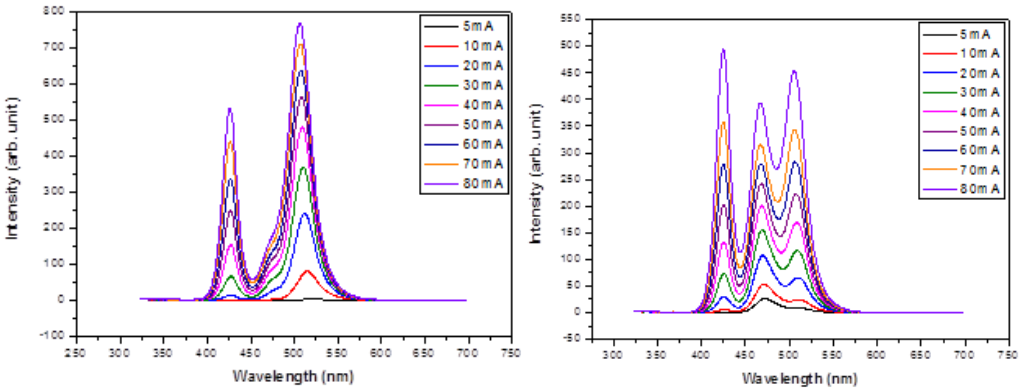

Figure 3.14: T-W MQWs EL spectrum with (left) p-GaN and (right) p-InGaN (AMDG Internal Document)

More interestingly, the change of In composition in the p-InGaN gives rise to results that are counter-intuitive. The following figure shows the same structure but with different indium composition (1.5%, 2% and 3%) in the p-type layer.

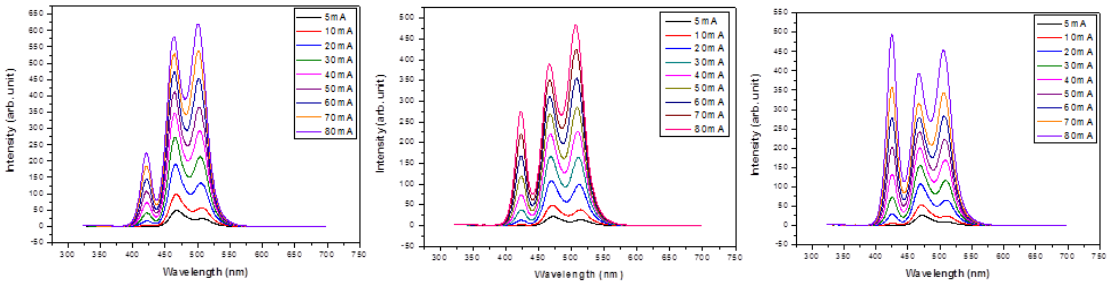

Figure 3.15: TW-MQWs EL spectrum with different In composition of the p-type layer : (left) 1.5%, (center) 2%, and (right) 3% (AMDG Internal Document)

When In composition increases, the last quantum well experiences an important augmentation of radiative recombination, while others remain approximately of a similar relative magnitude. Furthermore, several batches of this same structure have been fabricated, but show different EL results. The question is whether this difference is due to

growth condition change or fabrication process variation as the EL acquisitions have been done after device fabrication.

Therefore, the mechanisms responsible for this unexpected behavior are not understood and are currently under intense investigation.

3.9.2. TEGa and TMGa Precursors

TEGa and TMGa are typical precursors for Ga in MOCVD. No difference is experienced on the emitted intensity between using TEGa and TMGa for MQWs having a peak wavelength at around 500 nm. However, according to QuickTest EL results, there was an enhancement of intensity by using TEGa for MQWs emitting at 470 nm.

The improvement of intensity is about 19.6% when the injected current is 80 mA and 25% at 20 mA. But, this observation needs to be confirmed after device fabrication because metallic contact used before device fabrication are not of a good quality, possibly leading to inaccurate results.

3.9.3. Electron-Blocking Layer Study

This study is about using InAlN instead of AlGaN as an EBL. One problem with AlGaN EBL is that strain effects from lattice mismatch between the EBL and GaN from the active region can create strain-based piezoelectric fields in the active region. Further problems arise from the different spontaneous polarization fields. These fields act in a

sense that reduces the barrier's effectiveness. Adding more Al to the AlGaN to increase the bandgap, also increases these polarization field effects. It is also difficult to grow good-quality high-Al-content AlGaN layers. The optimum growth temperature for AlGaN can also be quite high, producing significant damage in the underlying layers, particularly for the high-In-content of InGaN in the active region.

InAlN can be lattice matched to GaN and InGaN, reducing the piezoelectric effects. In addition to having a larger energy bandgap, InAlN also has a large conduction-band offset relative to GaN (presenting a large barrier to electrons entering the p-type region) and relatively small valence-band offset (so that holes can get into the active region). Growth of InAlN also takes place at a lower temperature than AlGaN, leading to less damage to the active region. The following figure shows the improvement of performance by comparing different structures: InAlN composed of 18% of indium and grown at 845°C, AlGaN composed of 20% of aluminum and grown at 930°C and non-EBL structure with 20nm of p-GaN.

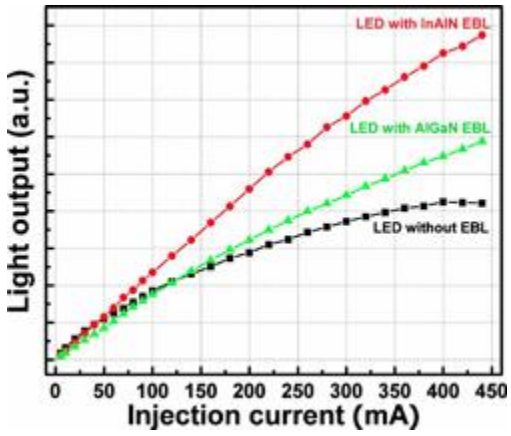

Figure 3.16: LED performances without EBL, with AlGaN and InAlN EBL (AMDG Internal Document)

Furthermore, a study of InAlN EBL epitaxial growth in our group [36] shows that a reduction of the growth temperature from 840°C to 780°C, along with a reduction of growth pressure (75 Torr instead of 300 Torr), leads to a stronger light emission. The following figure displays the integrated EL intensity results at different injection currents. LT-EBL refers to the EBL grown at low temperature (780°C) and HT-EBL to the one at 840°C. Plus, a conventional structure has been grown without EBL for reference purpose.

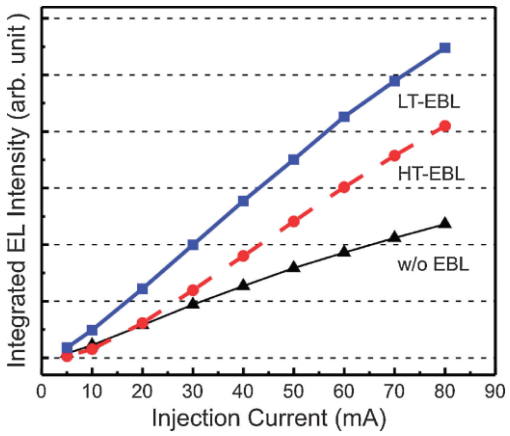

Figure 3.17: Integrated EL intensity function of injection current [36]

The higher efficiency at higher injection currents in the case of LT-EBL can be explained by a non-uniform layer thickness when grown at low temperature, enabling the holes to hop trough thinner regions of the EBL into the active region and then recombine radiatively with electrons. But, a higher peak wavelength shift compared to HT-EBL has been observed, probably due to hydrogen atoms (from nitrogen precursor NH_3 in MOCVD) diffusing from the p-layer to the QWs. This diffusion can be responsible for a reduction of the spontaneous polarization induced internal electric fields in the active

region as the positive hydrogen ions cancel the fixed negative charges at the InGaN/GaN interfaces. This reduction of internal fields can contribute to the good performance observed with LT-EBL as the non-uniform layer thickness may facilitate the hydrogen ions penetration into the active region.

3.9.4. Metallic Contact

Device fabrication has also been investigated. The main problem during device fabrication is to obtain a low ohmic contact resistance between the metal and the p-type layer. The previous fabrication process resulted in a contact resistance of 3.23e-3 Ω-cm^2, but the contact *I-V* curve was that of a Schottky barrier instead of an ohmic contact. The first study concerns the thickness of the metal layer, composed of nickel and silver. By decreasing the nickel layer thickness from previously 5 nm to 2 nm while keeping the silver one at 100 nm, the contact resistance has been lowered from 3.23e-3 Ω-cm^2 to 1.23e-3 Ω-cm^2. Furthermore, the contact is now ohmic.

The second improvement currently under investigation is related to the annealing temperature, where an optimal temperature of 550^{o}C instead of previously 500^{o}C may permit a further decrease of the metallic contact resistance.

4. EQUIPMENT FOR MEASUREMENT PURPOSE

All the results and improvements have been made possible thanks to the analysis of measurement data. AMDG has not only the equipment to grow materials but also the capability of carrying out almost all the required measurements on our LED devices, from material characterization to spectrum acquisition. The following list is not exhaustive, but gives an overview of the most important ones.

4.1. Electroluminescence

Electroluminescence (EL) is the phenomenon of light emission by radiative recombination due to injected carriers from an electrical current. The electrons injected to the n-type layer and the holes to the p-type layers propagate through their respective layer by diffusion. When they reach the active region, the electrons in the conduction band recombine with holes from the valence band. The energy lost during the de-excitation of the electron creates a photon. The emitted photons propagate with a wavelength associated to the bandgap energy (see equation 2.1).

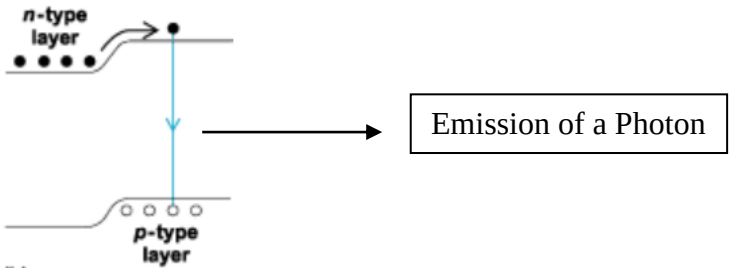

Figure 4.1: Illustration of radiative recombination process

Analyzing EL spectrum enables us to compare LED performance. Even if the light intensity is displayed in arbitrary units, comparing useful data such as peak intensity, peak wavelength, full-width half-maximum among others is of prime importance.

MQWs increase the probability of recombination; therefore the major peak will be ideally at a wavelength corresponding to the energy bandgap of these wells. However, the analysis of the EL measurement can display emission at other wavelengths which indicates an overflowing of the wells, or recombination at some other site in the material. Defects create nonradiative recombination centers and will thus degrade the EL performance of the device.

The EL equipment we are using is composed of a stage that supports the LED sample, a fiber optic cable, and two pins connected to a current source (Keithley 2430). The current source generates an electrical current in DC or pulse mode. The EL spectrum is acquired by a spectrometer (Ocean Optics HR2000) connected by USB to a computer. Below is a diagram of how light propagates through the optical bench of the HR2000 Spectrometer.

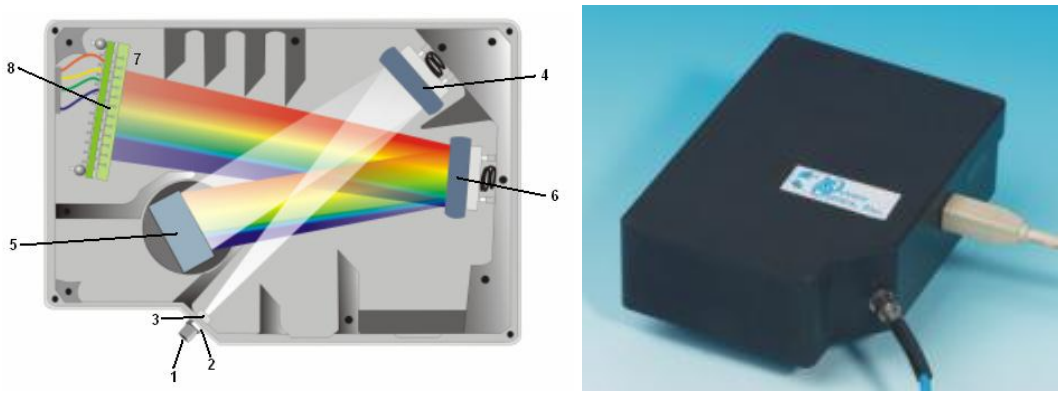

Figure 4.2: (left) Schematic and (right) picture of the HR2000 Spectrometer (HR2000 User's Manual)

The HR2000 Component Table on the following page explains the function of each numbered component in the HR2000 Spectrometer schematic.

Item	Name	Description
1	SMA Connector	Secures the input fiber to the spectrometer.
2	Slit	The size of the aperture regulates the amount of light that enters the optical bench and controls spectral resolution
3	Filter	Restricts optical radiation to pre-determined wavelength regions. Both bandpass and long-pass filters are available to restrict radiation to certain wavelength regions
4	Collimating Mirror	Focuses light entering the optical bench towards the grating of the spectrometer
5	Grating	Diffracts light from the Collimating Mirror and directs the diffracted light onto the Focusing Mirror
6	Focusing Mirror	Focuses the light onto the L2 Detector Collection Lens
7	L2 Detector Collection Lens	Focuses light from a tall slit onto the shorter CCD Detector elements
8	CCD Detector	Collects the light received from the L2 Detector Collection Lens and converts the optical signal to a digital signal. Each pixel on the CCD Detector responds to the wavelength of light that strikes it, creating a digital response

The spectrometer is controlled by a LabVIEW© program (QuickTest 2.0). More detail about this program will be provided in Chapter 6.

4.2. Photoluminescence

Photoluminescence (PL) is based on the same principle that EL but the difference is no carriers are electrically injected into the device. An optical source (usually a laser) acts

as an optical pump that excites electrons from the valence band to the conduction band through the absorption of the energy provided by the incoming beam of photons.

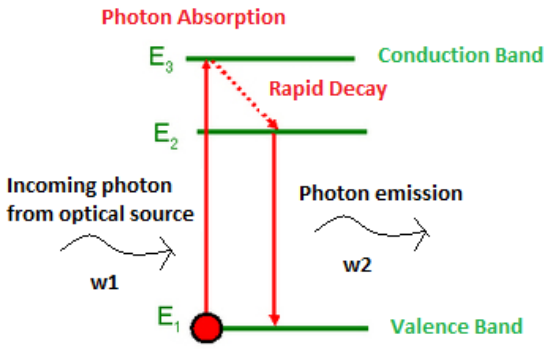

Figure 4.3: Illustration of photon generation by Photoluminescence

PL measurements permit the assessment of the performance of the active region. In contrary to EL measurements, metallic contacts and a p-type layer are not mandatory because no carriers are electrically injected, which gives us a way to specifically assess the quality of the active region as well as the MQW bandgap energy. The optical pump wavelength has to be shorter than the target wavelength of the emission in order to excite the electrons into the conduction band. However, a too short wavelength will enable radiative recombination in the n-GaN layer, which is not of interest for this measurement. Furthermore, the optical pump wavelength should be carefully chosen to enable radiative recombination in the QW but not in the quantum barriers.

A detector composed of a monochromator and an array of CCDs scans the spectrum and records the intensity at each wavelength. Since the measurements are carried out at ~300K and the material is not perfect, each peak will be broadened and thus have a

measurable line width. Sub-bandgap levels created by dopants and defects can result in photon emission which will broaden the spectrum or produce peaks of their own.

In the AMDG laboratories, PL measurements are performed by two different instruments. The first is an Accent RPM 2000 that provides a pump laser beam power of 2 mW at a wavelength of emission at 266 nm. The second is a more recent system that I have setup and which I have been assigned to supervise the measurement. It is more efficient for blue and green LED applications because the pump laser has an output power that is higher (20 mW) and emits at 325 nm which is closer to the target wavelengths, so it doesn't enable as much non-desired radiative recombination outside of QWs in the active region. The system is composed of a Helium-Cadmium laser used as the optical source, a cryostat that cools down the LED sample to 10 K for internal quantum efficiency assessment purpose (refer to Chapter 5), a focus lens setup, a triple-axis grating monochromator, and a CCD detector cooled down to -130^{o}C by liquid nitrogen.

4.3. Atomic Force Microscopy

Atomic force microscopy (AFM) is a very high-resolution type of scanning probe microscopy (SPM), with demonstrated resolution on the order of fractions of a nanometer. The first atomic force microscope was invented in 1986 by Binnig, Quate and Gerber, and the first commercially available one was introduced in 1989. The AFM is used for imaging, measuring, and manipulating matter at the nanoscale. For our applications, the AFM is operated as a sample surface imaging. The information is gathered by scanning the surface with a mechanical probe. Piezoelectric elements that

facilitate tiny but accurate and precise movements on command enable the very precise scanning.

In general, an AFM system is composed of five major components: a cantilever, probe tip, X-Y stage, laser, Position Sensitive Photo Diode (PSPD) and feedback mechanism.

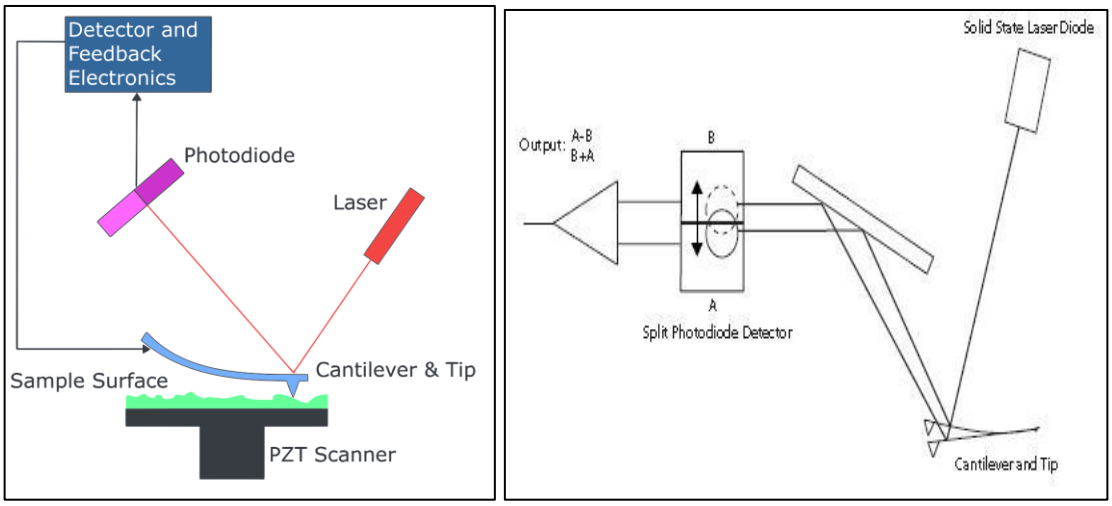

Figure 4.4: (Left) Overview of AFM system, (Right) Position detection mechanism [37]

When the sharp tip (made from silicon by micromachining) is scanned over a surface with feedback mechanism that enables the piezoelectric Z-scanner to maintain the tip at a constant force to obtain height information, the flexible cantilever under which the tip is attached moves up and down with the contour of the surface. A laser beam, focused on the back of reflective cantilever, is deflected toward the PSPD. The photodetectors measure the deflected light intensities and convert the cantilever motion into voltage and this is converted into height information using a differential amplifier.

The use of a feedback mechanism is due to the fact that if the tip was scanned at a constant height, a risk would exist that the tip collides with the surface, causing damage. Hence, a feedback mechanism is employed to adjust the tip-to-sample distance to maintain a constant force between the tip and the sample.

The sample is mounted on a piezoelectric stage that can move the sample in the *z* direction for maintaining a constant force, and the *x* and *y* directions for scanning the sample. The tip is mounted on a vertical piezoelectric scanner while the sample is being scanned in X and Y using another piezoelectric block. The resulting map of the area $z = f(x,y)$ represents the topography of the sample.

Scanners are characterized by their sensitivity which is the ratio of piezo movement to piezo voltage, i.e., by how much the piezo material extends or contracts per applied volt. Because of differences in material or size, the sensitivity varies from scanner to scanner. Sensitivity varies non-linearly with respect to scan size. Piezo scanners exhibit more sensitivity at the end than at the beginning of a scan. This causes the forward and reverse scans to behave differently and display hysteresis between the two scan directions. This can be corrected by applying a non-linear voltage to the piezo electrodes to cause linear scanner movement and calibrating the scanner accordingly.

AFM has three modes of operation: contact mode, non-contact mode and tapping mode. In contact mode, the force between the tip and the surface is kept constant during scanning by maintaining a constant deflection thanks to the feedback mechanism. The tip and the surface are actually in contact which means the necessity of having a hard sample surface in order to not deteriorate the sample. In non-contact mode, the tip of the

cantilever does not contact the sample surface. The cantilever is instead oscillated at a frequency slightly above its resonant frequency. The van der Waals forces, which are strongest from 1 nm to 10 nm above the surface, or any other long range force which extends above the surface acts to decrease the resonance frequency of the cantilever.

This decrease in resonant frequency combined with the feedback loop system maintains a constant oscillation amplitude or frequency by adjusting the average tip-to-sample distance.

Measuring the tip-to-sample distance at each (x,y) data point allows the scanning software to construct a topographic image of the sample surface. In tapping mode, the idea is to keep the probe tip close enough to the sample for short-range forces to become detectable while preventing the tip from sticking to the surface. The cantilever is in tapping mode driven to oscillate at near its resonance frequency by a small piezoelectric element mounted in the AFM tip holder similar to non-contact mode. However, the amplitude of this oscillation is greater than 10 nm, typically 100 to 200 nm. Due to the interaction of forces acting on the cantilever when the tip comes close to the surface, Van der Waals force, dipole-dipole interaction, electrostatic forces, etc., cause the amplitude of this oscillation to decrease as the tip gets closer to the sample. An electronic servo uses the piezoelectric actuator to control the height of the cantilever above the sample. The servo adjusts the height to maintain a set cantilever oscillation amplitude as the cantilever is scanned over the sample. A tapping AFM image is therefore produced by imaging the force of the intermittent contacts of the tip with the sample surface.

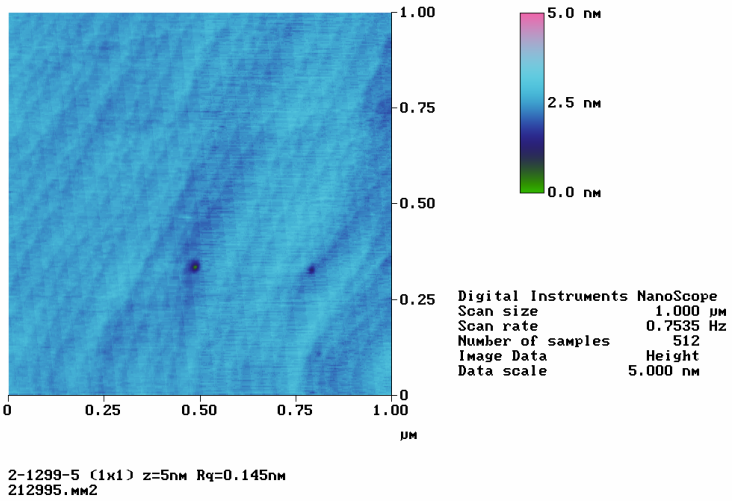

Figure 4.5: AFM Image of a GaN surface with scale, scan parameters and data result (AMDG Internal Document)

The AFM used by the group is a Veeco Dimension 3100 scanning probe microscope operated in tapping mode. High resolution scans are obtained at 5 x 5 μm^2. This equipment is available in the MiRC.

4.4. Transfer Length Measurement

Transfer Length Measurement (TLM) is a technique used to determine the contact resistance between a metal and a semiconductor. The technique involves making a series of metal-semiconductor contacts separated by various distances. Probes are applied to pairs of contacts, and the resistance between them is measured by applying a voltage across the contacts and measuring the resulting current. The current flows from the first

probe into the metal contact, across the metal-semiconductor junction, through the sheet of semiconductor, across the metal-semiconductor junction again into the second contact, and from there into the second probe and into the external circuit to be measured by a current meter. The resistance measured is a sum of the contact resistance of the first contact, the contact resistance of the second contact, and the sheet resistance of the semiconductor in-between the contacts.

If several such measurements are made between pairs of contacts that are separated by different distances, a plot of resistance versus contact separation can be obtained. The contact separation is expressed in terms of *L* (gap between 2 contacts). *W* is the width of the area between the contacts. Ideally, the plot should be linear and the result of the multiplication between the slope of the line and the width *W* is the sheet resistance. The intercept of the line with the y-axis, is two times the contact resistance. Thus the sheet and contact resistance can be determined from this technique.

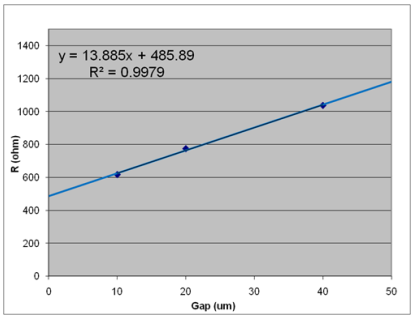

R_{sh} = 2.78 kΩ/sq

R_c = 242.5 Ω

Figure 4.6: Example of TLM result (AMDG Internal Document)

4.5. Hall-Effect measurement

The Hall effect is the generation of a voltage difference (the Hall voltage) across an electrical conductor, transverse to an electric current in the conductor and a magnetic field perpendicular to the current. It was discovered by Edwin Hall in 1879.

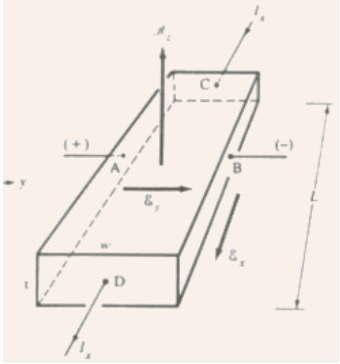

Figure 4.7: Illustration of Hall effect in a p-type bar [38]

If a magnetic field is applied perpendicular to the direction in which carriers drift in a semiconductor, the path of the carriers tends to be deflected. The total force $\boldsymbol{F}$ (Newton) on a single carrier due to the electric and magnetic fields is:

$$\boldsymbol{F} = q(\boldsymbol{E} + \boldsymbol{v}\mathrm{x}\boldsymbol{B}) \qquad (4.1)$$

Where q is the magnitude of the electronic charge (Coulomb), v the drift velocity of the carrier ($m.s^{-1}$), $\boldsymbol{B}$ the magnetic field vector (Tesla) and E the electric field ($N.C^{-1}$).

In the y-direction, the force is:

$$F_y = q\left(E_y - v_x B_z\right) \qquad (4.2)$$

Thus, a force represented by qv_xB_z is experienced in the $-y$ direction. To maintain a steady state flow of carriers (holes in this example) down the length of the bar, the electric field E_y must balance the product v_xB_z:

$$E_y = v_x B_z \qquad (4.3)$$

$$E_y = (J_x/q.p_0) B_z \qquad (4.4)$$

After some calculations, the hole concentration is:

$$p_0 = \frac{I_x B_z}{q\ t\ V_{AB}} \qquad (4.5)$$

With p_0 the hole concentration (cm^{-3}), I_x the electrical current (A), t the thickness of the material (cm), and V_{AB} the Hall Voltage (V).

In practice, the Hall coefficient (R_H) is usually used to derive carrier concentration and mobility:

$$R_H = \frac{V_{AB} \,.\, t}{I_x \,.\, B_z} \qquad (4.6)$$

For n-type materials, the calculations are the same, except that the magnitude of the electronic charge (q), the Hall voltage V_{AB} and the Hall coefficient R_H are negative.

The measurement is carried out using an Accent HL5500PC Hall-effect system where a 1x1 cm^{-1} square sample is prepared by depositing an ohmic contact to each corner

(labeled 1-2-3-4). Free-standing resistivity is measured by applying a current across one pair of contacts and measuring the voltage across the other pair in the two configurations as per the following equation:

$$\rho = 2.266.\mathrm{t}.\left(\frac{V_{43}}{I_{12}} + \frac{V_{23}}{I_{14}}\right).\mathrm{F} \qquad (4.7)$$

where *t* is the sample thickness, *I* is the applied current, *V* is the measured voltage, and *F* is a correction factor based on sample symmetry (1 for a perfect square).

4.6. X-Ray Diffraction (XRD)

X-rays are electromagnetic radiation with typical photon energies in the range of 100 eV to 100 keV. For diffraction applications, only short-wavelength X-rays in the range of a few angstroms to 0.1 angstrom (1 keV - 120 keV) are used. Because the wavelength of X-rays is comparable to the size of atoms, they are ideally suited for probing the structural arrangement of atoms in a wide range of materials. The energetic X-rays can penetrate deep into the materials and provide information about the structural properties, such as composition and uniformity of epitaxial layers, thickness, built-in strain and strain relaxation, and crystalline perfection related to the dislocation density.

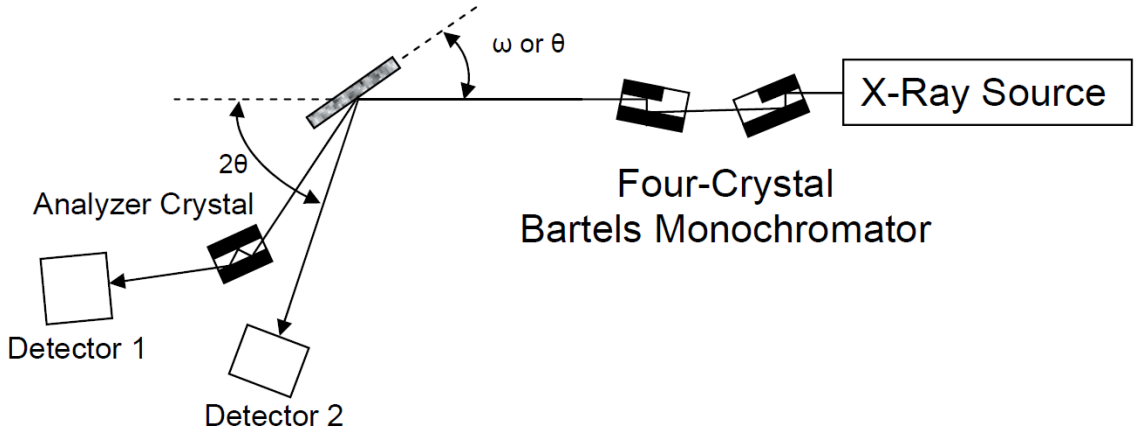

Figure 4.8: Schematic of an XRD system [5]

X-rays are produced generally by either X-ray tubes or synchrotron radiation. In a X-ray tube, which is the primary X-ray source used in laboratory X-ray instruments, X -rays are generated when a focused electron beam accelerated across a high voltage field bombards a stationary or rotating solid target. As electrons collide with atoms in the target and slow down, a continuous spectrum of X-rays are emitted, which are termed Bremsstrahlung radiation. The high energy electrons also eject inner shell electrons in atoms through the ionization process. When a free electron fills the shell, a X-ray photon with energy characteristic of the target material is emitted. Common targets used in X-ray tubes include Cu and Mo, which emit 8 keV and 14 keV X-rays with corresponding wavelengths of 1.54 Å and 0.8 Å, respectively.

In recent years, synchrotron facilities have become widely used as preferred sources for X-ray diffraction measurements. Synchrotron radiation is emitted by electrons or positrons travelling at near light speed in a circular storage ring. These powerful sources,

which are thousands to millions of times more intense than laboratory X-ray tubes, have become indispensable tools for a wide range of structural investigations.

X-rays primarily interact with electrons in atoms. When X-ray photons collide with electrons, some photons from the incident beam will be deflected away from the direction where they originally travel. If the wavelength of these scattered X-rays did not change (meaning that X-ray photons did not lose any energy), the process is called elastic scattering (Thompson Scattering) in that only momentum has been transferred in the scattering process. These are the X-rays that we measure in diffraction experiments, as the scattered X-rays carry information about the electron distribution in materials. On the other hand, in the inelastic scattering process (Compton Scattering), X-rays transfer some of their energy to the electrons and the scattered X-rays will have different wavelength than the incident X-rays.

Diffracted waves from different atoms can interfere with each other and the resultant intensity distribution is strongly modulated by this interaction. If the atoms are arranged in a periodic fashion, as in crystals, the diffracted waves will consist of sharp interference maxima (peaks) with the same symmetry as in the distribution of atoms. Measuring the diffraction pattern therefore allows us to deduce the distribution of atoms in a material.

The peaks in an X-ray diffraction pattern are directly related to the atomic distances. For a given set of lattice planes with an inter-plane distance of d_{hkl}, the condition for a diffraction (peak) to occur can be simply written using the Bragg's law:

$$2\, d_{hkl}\, sin(\theta_B) = n\lambda \qquad (4.8)$$

For a Bravais Lattice:

$$\frac{1}{d^2{}_{hkl}} = \frac{4}{3}\left(\frac{h^2 + hk + k^2}{a^2}\right) + \frac{l^2}{c^2} \qquad (4.9)$$

where λ is the wavelength of the x-ray, θ_B the scattering angle, *n* is an integer representing the order of the diffraction peak, *(hkl)* are the Miller indices of the crystal, and *a and c* Bravais lattice constants.

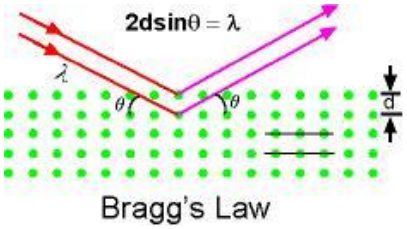

Figure 4.9: Illustration of the Bragg's law in the case of a 2D lattice plan [39]

Thin film diffraction is used to characterize thin film samples grown on substrates. There are several special considerations for using XRD to characterize thin film samples. At first, reflection geometry is used for these measurements as the substrates are generally too thick for transmission.

Secondly, high angular resolution is required because the peaks from semiconductor materials are sharp due to very low defect densities in the material. Consequently, multiple bounce crystal monochromators are used to provide a highly collimated X-ray beam for these measurements. For example, in the Philips X'PERT MRD used in our lab,

a four-crystal monochromator made from Ge (220) is used to produce an incident beam with 0.00001^{o} of angular resolution.

Precise lattice constant measurements provide information about lattice mismatch between the film and the substrate, and therefore are indicative of strain and stress. Superlattice measurements in multilayered heteroepitaxial structures, which manifest as satellite peaks surrounding the main diffraction peak from the film are used to measure film thickness and quality.

But, the most commonly scan technique used is the rocking-curve measurement in which a ω scan at a fixed 2θ angle is carried out. In this configuration, the detector is kept at a fixed angle relative to the primary beam (2θ) while the sample is rotated or "rocked" across the ω axis (refer to Figure 4.8). Rocking curves are useful for determining the c lattice constant via the following equation:

$$c = \frac{n\lambda l}{2\,sin(\theta)} \qquad (4.10)$$

In a perfect crystal with no strain or defects, the ω-scan produces a δ-function at the Bragg angle. But in the presence of imperfect plane spacing, the Bragg peak is broadened. The full width half maximum (FWHM) of this broadened peak is useful for comparing the relative quality of different samples. Asymmetric rocking curves on planes can provide more information since the FWHM of these Bragg peaks are sensitive to threading dislocations [40, 41].

The following graph shows a high-resolution XRD data. The structure under measurement is a conventional LED structure composed of 5 InGaN (2.5 nm) / GaN (12 nm) MQWs emitting at 500 nm, GaN:Si^{+} n-type layer (3 μm), and two different p-type layers (p-GaN for reference and p-$In_{0.02}Ga_{0.98}N$).

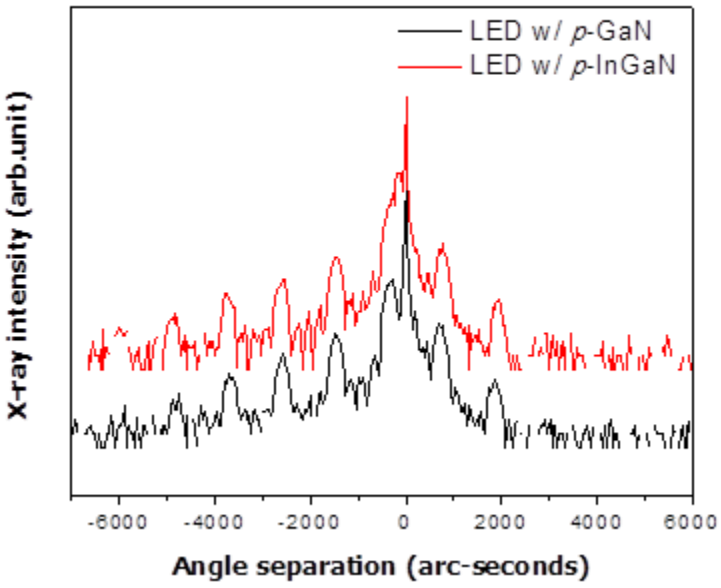

Figure 4.10: Data result from XRD measurement: Conventional LED structure with (bottom) p-GaN and (top) p-InGaN (AMDG Internal Document)

5. TEMPERATURE-DEPENDENT PHOTOLUMUNESCENCE

The following sections (Chapters 5 and 6) describe the actual work I have done while in the AMDG. They are ordered in a chronological order, beginning with a Photoluminescence measurement station I have setup to provide temperature-dependent PL data in order to primarily determine the internal quantum efficiency (IQE) of our LED structures. The IQE is the ratio of the photons emitted from the active region to the number of electrons photogenerated into the LED structure. The assumption is at very low temperature, every photogenerated electron gives birth to a photon, which leads to 100% IQE. But, as the temperature increases, nonradiative recombination occurs in the active region due to defect sites that are thermally activated, as well as other effects we have discussed related to the efficiency droop.

Therefore, the IQE gives us a good way to compare the quality of the MQW structure of different samples. An IQE of 100% means that the crystal is perfect (no defects) and only radiative recombination occurs. But, in practice, the IQE determined at 300K in our LED structures is about 35 % for peak wavelengths around 525 nm and roughly 50 % for 490 nm. The measurement has been carried out for mostly MQW active regions and no p-type layer.

5.1. Preliminary

Temperature-Dependent Photoluminescence (TD-PL) is a technique used to acquire the spectrum from samples when optically excited at different temperatures.

As introduced in section 4.2, Photoluminescence (PL) is the spontaneous emission of light from a material under optical excitation. PL analysis is nondestructive because the technique requires very little sample manipulation or environmental control. Because the sample is excited optically, electrical contacts and junctions are unnecessary and high-resistivity materials pose no practical difficulty. When light of sufficient energy is incident on a material, photons are absorbed and electronic excitations are created. Eventually, these excitations relax and the electrons return to the ground state, or valence band. If radiative relaxation occurs, the emitted light is called PL. The PL spectrum provides the transition energies, which can be used to determine electronic energy levels. The PL intensity gives a measure of the relative rates of radiative and nonradiative recombination. Compared with other optical methods of characterization like reflection and absorption, PL is less stringent about beam alignment, surface flatness, and sample thickness.

For our application, the first objective is to determine the internal quantum efficiency by comparing the integrated intensity of emission at different temperatures (10 K to 310 K with a 20 K step) thanks to a temperature-controlled cryostat system. The following diagram shows the setup of the TD-PL system.

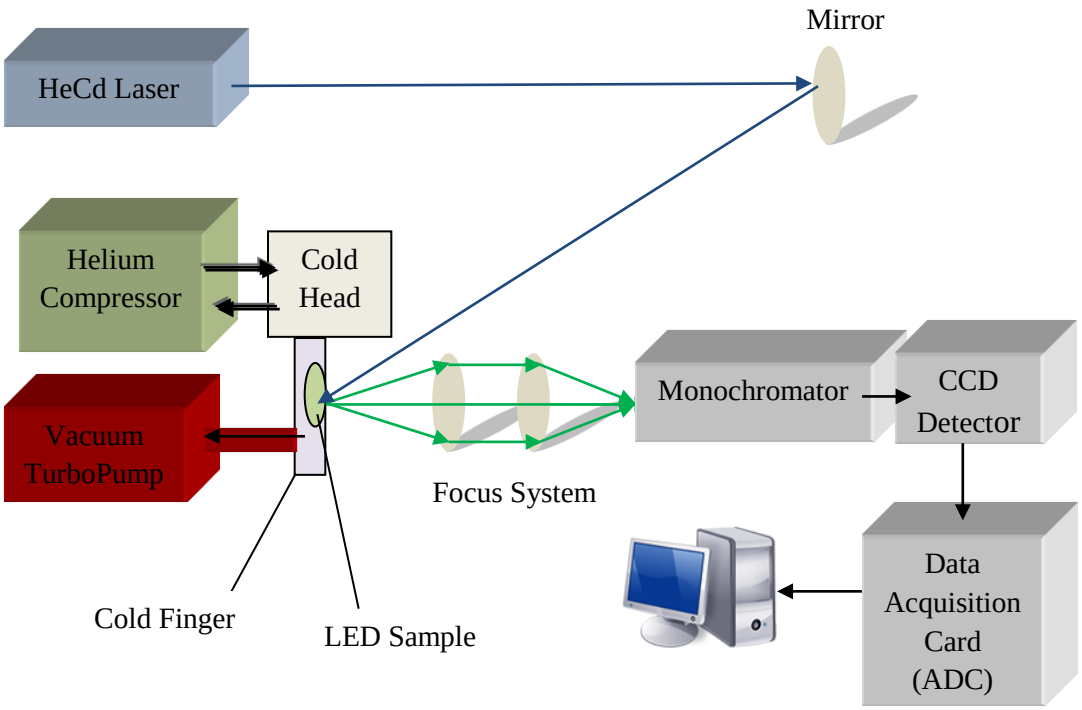

Figure 5.1: Schematic diagram of the TD-PL setup

5.2. Optical pump

The choice of excitation is critical in any PL measurement. The excitation energy and intensity will have profound effects on the PL signal. Because the absorption of most materials depends on energy, the penetration depth of the incident light will depend on the excitation wavelength. Hence, different excitation energies probe different regions of the sample. The excitation energy also selects the initial excited state in the experiment. Because lasers are monochromatic, intense, and readily focused, they are the instruments of choice for PL excitation. For our applications, the excitation power is not critical as the active region of the samples under measurement is the first region that the laser strikes. Indeed, many of the samples used for PL measurements are grown without a p-type layer,

which enables the laser to excite all of the QWs in the active region. This has been proved by using a Triple Wavelength-MQW where the emission of three peak wavelengths corresponding to the three QWs has been observed.

The excitation source, or optical pump, is a Helium Cadmium (HeCd) Series 74 laser produced by Melles Griot.

Figure 5.2: Picture of a HeCd Series 74 laser
(Courtesy to Dong-A University)

The principle of functioning of helium cadmium lasers is a complex electrical discharge that produces output in the ultraviolet (325 nm) and a power of 25 mW. The basic medium of the discharge is helium (a gas), but the lasing component is cadmium (a metal). To obtain stable laser action, the cadmium must first sublimate into a quasi-gaseous form and then be evenly distributed throughout the helium discharge through the processes of diffusion and cataphoresis.

5.3. Cryostat

The cryostat system is used to control and monitor the sample temperature. It is composed of a helium compressor, cold head, cold finger, temperature sensor, heater and temperature controller. The sample can be cooled down to 10 K in approximately

40 minutes. The advantage of this system is that helium gas flows in a closed-loop, which means there is no need of recharging the helium reservoir.

The compressor is a single-stage, water-cooled, rotary compressor designed to deliver high-pressure, oil-free helium gas to the cold head. The optimal pressure is around 260 psi and the gas is 99.995% pure. The purpose of the compressor is to cool the gas through three–circuit heat exchangers, remove oil and moisture and pressurize (compress) the helium gas.

Then, the helium gas is sent to the cold head to cool down the cold finger where the samples are attached to. The system is based on Gifford-McMahon refrigeration cycle, where the helium gas absorbs heat by expansion on heat stations in the cold head. The cold created by this mean is transferred to the sample holder in the cold finger.

A vacuum turbopump is used to create vacuum in a vacuum jacket where the sample-holder is located in order to prevent thermal transfer and to avoid the creation of ice from air moisture inside the system.

A heater plugged in the sample holder and controlled by a temperature controller along with a GaAs diode sensor enables a control and monitoring of the sample temperature.

Thanks to this system, the spectrum acquisition is done from 10 K to 310 K with a 20 K step.

5.4. Spectrum Acquisition

Because the emission from the sample is isotropic, a focus system is required to focus the light into a small spot that enters the monochromator. The monochromator (Triax 190) functioning is based on diffraction, using a triple axis grating turret fitted with a

visible-blaze diffraction grating having 1200 grooves/mm to spatially separate the colors of light.

The optical system is designed according to the Czerny-Turner design (refer to Figure 5.3). The broad band illumination source (**A**) enters the monochromator at the entrance slit (**B**). The amount of light energy available for use depends on the intensity of the source in the space defined by the slit (width x height) and the acceptance angle of the optical system. The slit is placed at the effective focus of a curved mirror (the collimator, **C**) so that the light from the slit reflected from the mirror is collimated (focused at infinity). The collimated light is diffracted from the grating (**D**) and then is collected by another mirror (**E**) which refocuses the light, now dispersed, on the exit slit (**F**). At the exit slit, the colors of the light are spread out. Because each color arrives at a separate point in the exit slit plane, there are a series of images of the entrance slit focused on the plane. Because the entrance slit is finite in width, parts of nearby images overlap. The light leaving the exit slit (**G**) contains the entire image of the entrance slit of the selected color plus parts of the entrance slit images of nearby colors. A rotation of the grating causes the band of colors to move relative to the exit slit, so that the desired entrance slit image is centered on the exit slit. The range of colors leaving the exit slit is a function of the width of the slits. The entrance and exit slit widths are adjusted together. The resolution of the instrument is determined by measuring the FWHM, which is inferior to 0.2 nm in our system.

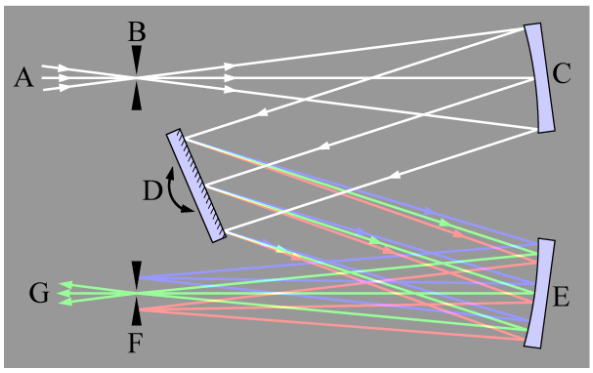

Figure 5.3: Illustration of a Czerny-Turner design [42]

Then, a CCD detector transforms the incoming light into an analog voltage. As very low thermal noise is required for our application, the detector is cooled using liquid nitrogen through a 1 liter reservoir (capable of reaching -130^{o}C and lasts about 24 hours). The voltage is then digitalized through an Analog to Digital Converter (ADC) before being formatting into a data acquisition card connecting to a computer. The spectrum scanned during this process is from 200 nm to 1200 nm, but the actual data used by the group is from 350 nm to 650 nm.

5.5. TD-PL data result

The following results show the measurement data of the LED sample no. 2-2506-3 with a conventional MQW structure, composed of 5 InGaN quantum wells.

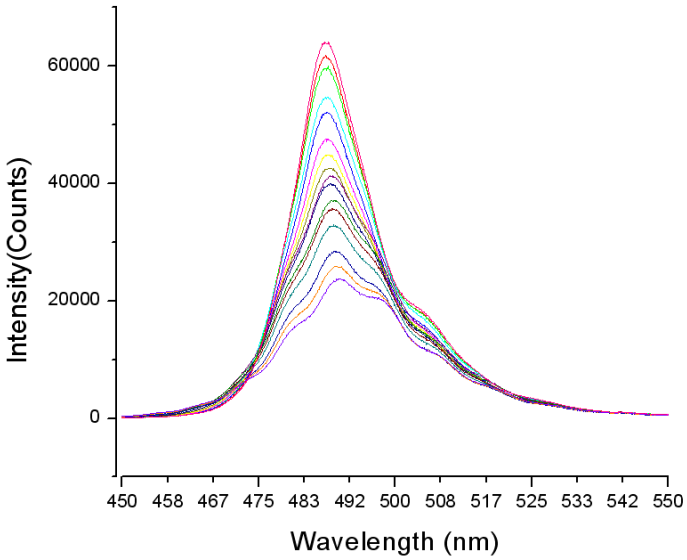

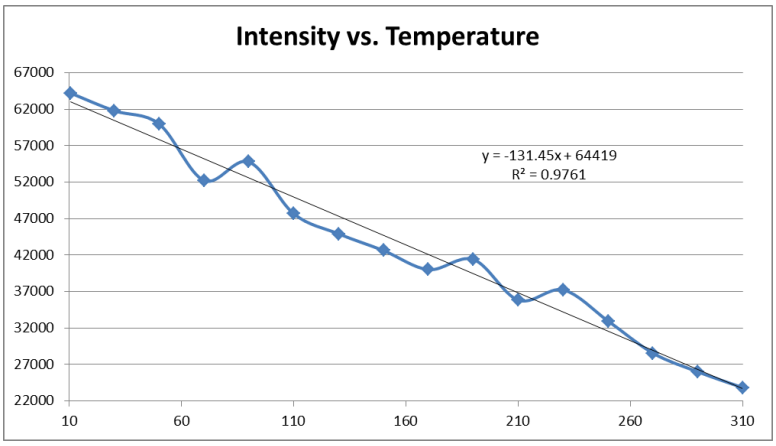

Figure 5.4: (Top) TD-PL and (bottom) intensity function of temperature of the sample

This previous figure shows an overlaid graph of PL measurement at different temperatures. At first, one can notice that a factor of 3 exists between the peak intensities at the minimum (10.75 K) and maximum (310 K) temperatures, which prove a strong temperature dependence of nonradiative recombination.

Then, a "red-shift" trend is experienced when increasing temperature. This is explained from Varshni formula:

$$E_g = E_{g_{T=0K}} - \frac{\alpha T^2}{T + \beta} \qquad (5.1)$$

Where α and β are Varshni fitting parameters. The energy bandgap reduces with increasing temperature, explaining the "red-shift" phenomenon. In case of InGaN [43]:

$$E_{g_{T=0K}} = 2.55\ eV\ , \quad \alpha = 8.32\ x\ 10^{-4}\ \frac{eV}{K}\ , \quad and \quad \beta = 835.6\ K$$

Hence:

$$\lambda\ (T) = \frac{h\ x\ c}{E_{g_{(T)}}} = \frac{h\ x\ c}{E_{g_{T=0K}} - \frac{\alpha\ T^2}{T + \beta}} \qquad (5.2)$$

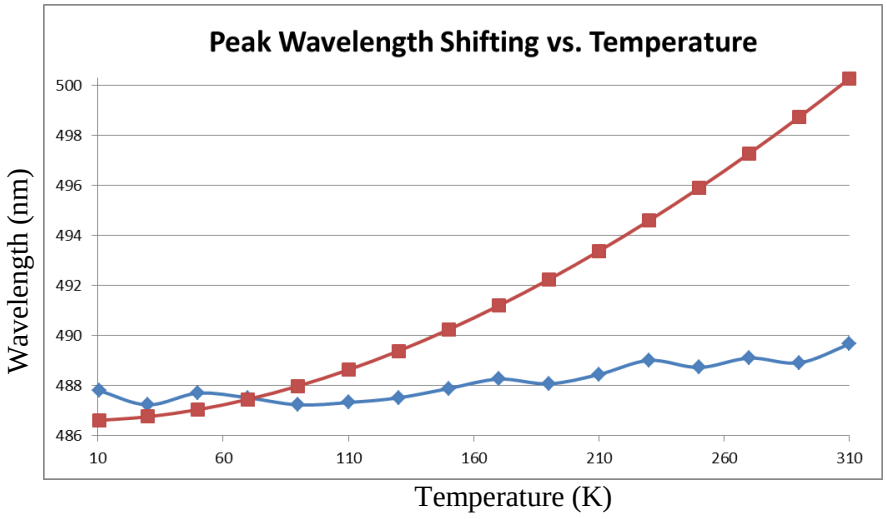

Figure 5.5: (Red □) Simulation using Varshni formula and (Blue ◊) measured peak wavelength shift

The difference between the Varshni simulation and the measured shift is due to InGaN localization, combined with inexact Varshni coefficients as they depend of In composition in the alloy and have to be determined experimentally.

InGaN localization plays a role in the shift of the central wavelength as well as broadening the spectrum. Indium has a tendency to not be uniformly distributed in InGaN material but rather forms clusters, and temperature gradients across the substrate can lead to segregation of indium which causes localized potential minima [35]. Since higher indium content means lower bandgap, a non-uniform distribution of energy potentials will form across quantum well layers and photons of different energy (and thus different wavelength) will be emitted from different parts of the wafer.

At a temperature lower than 70 K, the carriers have not enough energy to pass over potential fluctuations, therefore the radiative recombination occurs at the same position where electron-hole pairs have been generated. But, with increased temperature until around 150 K, carriers are able to overcome potential fluctuations and relax into lower potential minima where the indium composition is higher, leading to a red-shifted spectrum of emission. Then, if the temperature keeps increasing, the lower bandgap energy states will be populated, so a delocalization out of potential minima occurs and results in blue-shift. This process is referred as “S-shape” temperature dependence of the peak intensity [43].

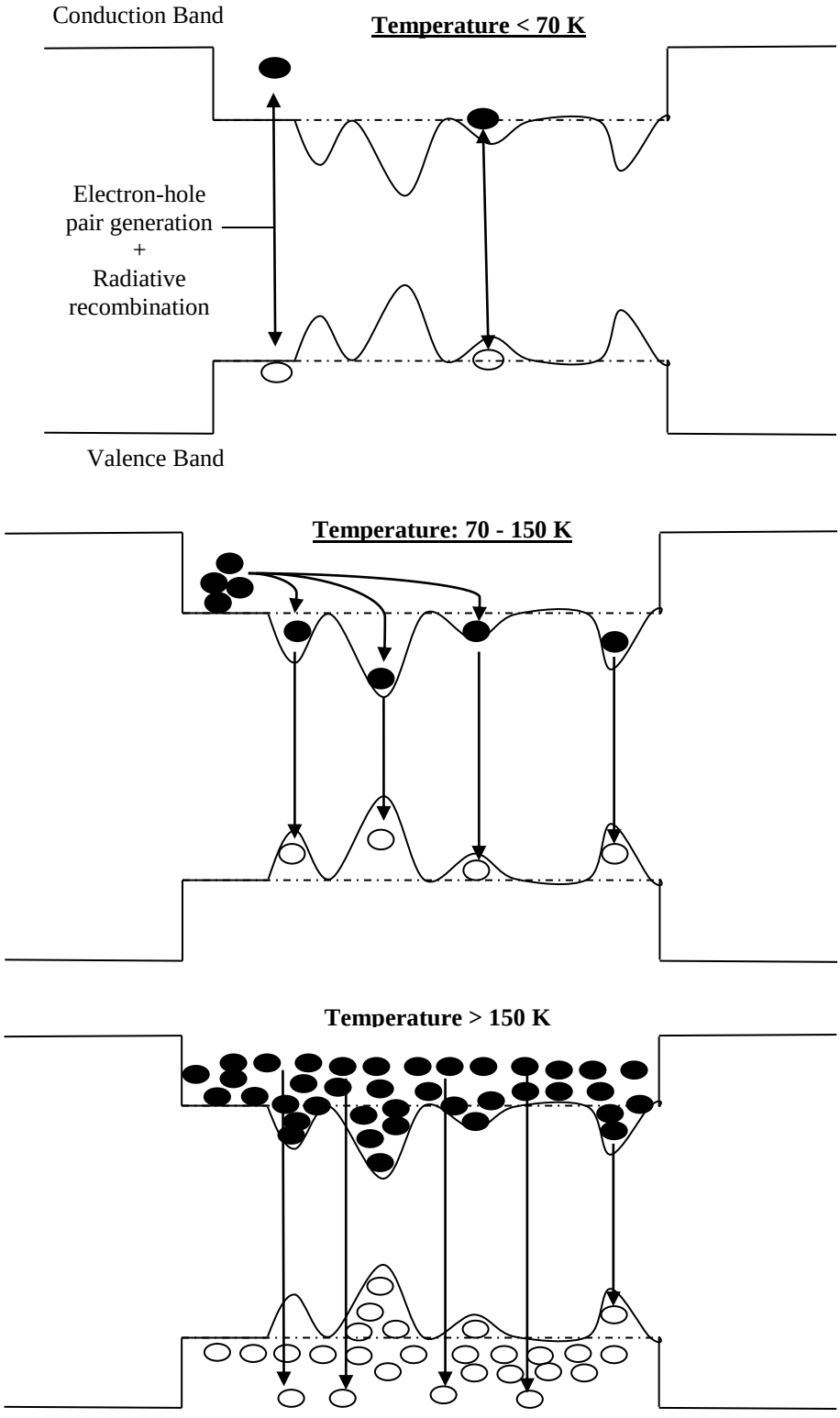

Figure 5.6: Illustration of indium localization effect

Localized potential minima prevent carriers from reaching dislocations and instead recombine radiatively. By this means, indium localization enhances photon emission and so improves brightness. But, the growth of high-quality InGaN becomes increasingly more difficult as the In composition increases. In fact, lattice-mismatch resulting in increasing polarization effect and poor crystal quality become predominant and so degrade performances.

Studies show that indium localization improves brightness for blue LEDs, but degrades efficiency when approaching green wavelengths [44, 35].

Another data result of interest is the linewidth, or Full-Width Half Maximum (FWHM). This is an assessment of the crystal purity as impurities create defect sites, resulting in allowing energy states in the forbidden band where electrons can be trapped and emit photons at different wavelengths. This can be observed in the emission spectrum of an LED via a broadening of the linewidth from the central peak wavelength, and calculated by determining the distance (in nm) between the right and left edges of the spectrum at half maximum of the peak intensity.

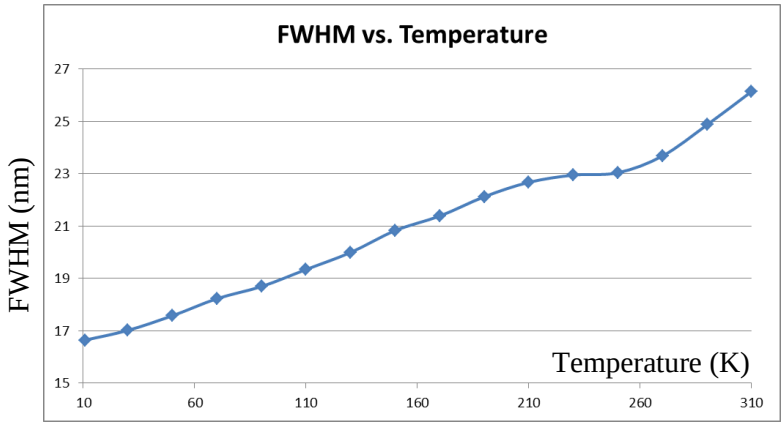

Figure 5.7: FWHM result of the sample no. 2-2506-3

However, the principal data result of PL measurement is the IQE. In theory, the intensity decreases linearly with temperature. But in practice, it is not perfectly linear due to temperature control issues. In fact, the sample is attached to a sample-holder in the cold finger. The sample-holder is equipped with a temperature sensor (GaAs diode) and a heater, which are the fundamentals elements for temperature control and monitoring. Therefore, the temperature of the sample-holder is quite well controlled and known, but the thermal contact between the sample-holder and the actual sample is done using a thin layer of Apiezon N grease, which improves the contact compared to copper tape but its efficiency is nonetheless not accurately known. Thus, a difference exists between the displayed temperature and the actual sample temperature. Therefore, a linear regression curve fitting is used on the raw data in order to correct this issue.

The IQE is calculated by the following equation:

$$IQE = \frac{Integrated\ Intensity\ (T1) - Integrated\ \ Intensity\ (T2)}{T1 - T2} \tag{5.3}$$

Where *T1* and *T2* are temperatures and the intensity is integrated from 350 to 650 nm. In our case, the temperatures chosen for the IQE calculation are the minimum (10.75 K) and the maximum (310 K). The following figures show the integrated intensity function of temperature and the corresponding IQE.

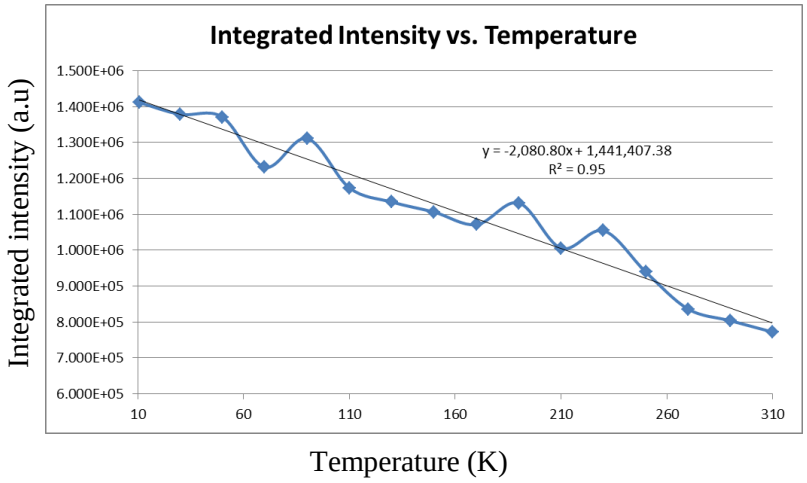

Figure 5.8: Integrated intensity function of temperature for IQE calculation

Raw IQE (%)	54.68
IQE Linear (%)	56.12

Figure 5.9: IQE results for the sample no. 2-2506-3

As expected, the raw IQE (using raw integrated intensity data) and the linearized one are different, but the difference is quite insignificant. However, one of the problems to overcome before reaching this result was to improve the thermal contact between the sample and sample-holder because the difference was previously higher, around 8 %. The previous samples were mounted using copper tape instead of grease. The following figures show the results with copper tape.

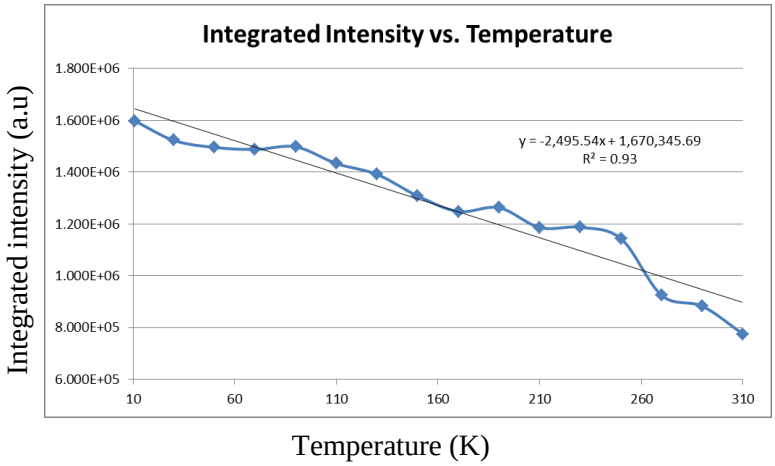

Raw IQE (%)	48.49
IQE Linear (%)	54.57

Figure 5.10: Example of (Top) a TD-PL and (bottom) IQE result using copper tape

The thermal contact is highly improved when using the grease as we can notice from the graph and IQE result where the difference between the raw data and the linearized one is only about 1.4 % compared to around 6 % for the previous result.

So far, the maximum IQE measured is 56 % (sample 2-2506-3, 490 nm peak wavelength with a MQW) and the minimum is 26 % (sample 2-2461-3, 525 nm peak wavelength with a MQW).

In conclusion, the results confirm that when one approaches the green wavelengths, an important decrease of the IQE is experienced, from 50 % for cyan LEDs (around 490 nm) to 35 % for close green LEDs (525 nm), due to the efficiency reduction experienced when approaching green wavelengths.

6. QUICKTEST 2.0

The software, named QuickTest 2.0, is a program based on the G language used by LabVIEW©, an integrated development environment developed by National Instruments. The choice of using LabVIEW© comes from the fact that the previous software was already a LabVIEW© program, and also because it is easier and faster to create a program with LabVIEW© for instrument control rather than text-based programs such as C/C++ or Visual Basic. Besides, as the communication between the computer and the current source is using GPIB (General Purpose Interface Bus), LabVIEW© has built-in functions for GPIB communication that makes the programming easier.

6.1. LabVIEW

LabVIEW© stands for LABoratory Virtual Instrument Engineering Workbench. It is a programming environment in which programs are created with graphics. It is designed for scientists and engineers, who need to program as part of their jobs. The graphical programming language called G enables the users to create programs in a pictorial form called a block diagram, eliminating a lot of the syntactical details. LabVIEW© uses terminology, icons, and ideas familiar to scientists and engineers. It relies on graphical symbols rather than textual language to describe programming actions. The core of the G language is based on the principle of dataflow, in which functions execute only after receiving the necessary data, governs execution in a straightforward manner.

LabVIEW© programs are called Virtual Instruments (VIs) because their appearance and operation imitate actual instruments. VIs has primarily two main parts.

The front panel is the interactive user interface of a VI, so named because it simulates the front panel of a physical instrument. It can contain knobs, push buttons, graphs, and many other controls (which are user inputs) and indicators (which are program outputs).

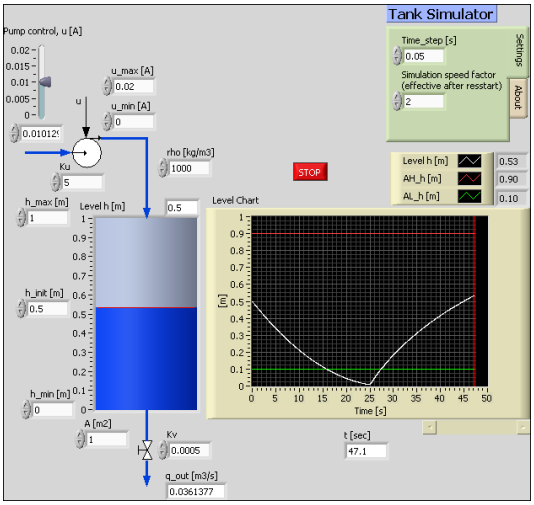

Figure 6.1: Example of a front panel [45]

The second is the block diagram where the source code is located. It is the actual executable program. The components of a block diagram are lower-level VIs, built-in functions, constants, and program execution control structures. Wires are drawn to connect the appropriate objects together to indicate the flow of data between them. Front panel objects have corresponding terminals on the block diagram so data can pass from the user to the program and back to the user.

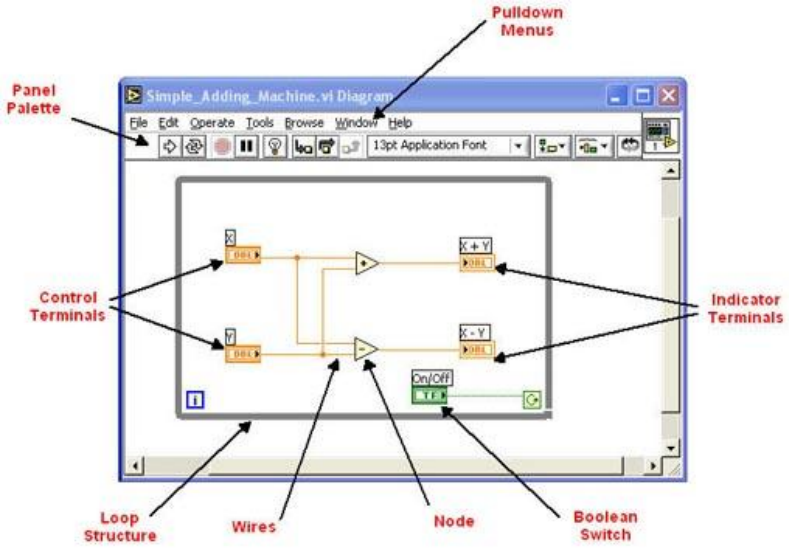

Figure 6.2: Example of a block diagram [46]

6.2. Motivation

The motivation was to replace the previous software that was not optimized for Electroluminescence application. In fact, the previous version (QuickTest) was programmed with an older version of LabVIEW©, and was designed for various applications in one program. Besides, the program suffered from containing an excessive number of programming structures, which slowed down the measurement. The following figure shows the EL measurement station setup.

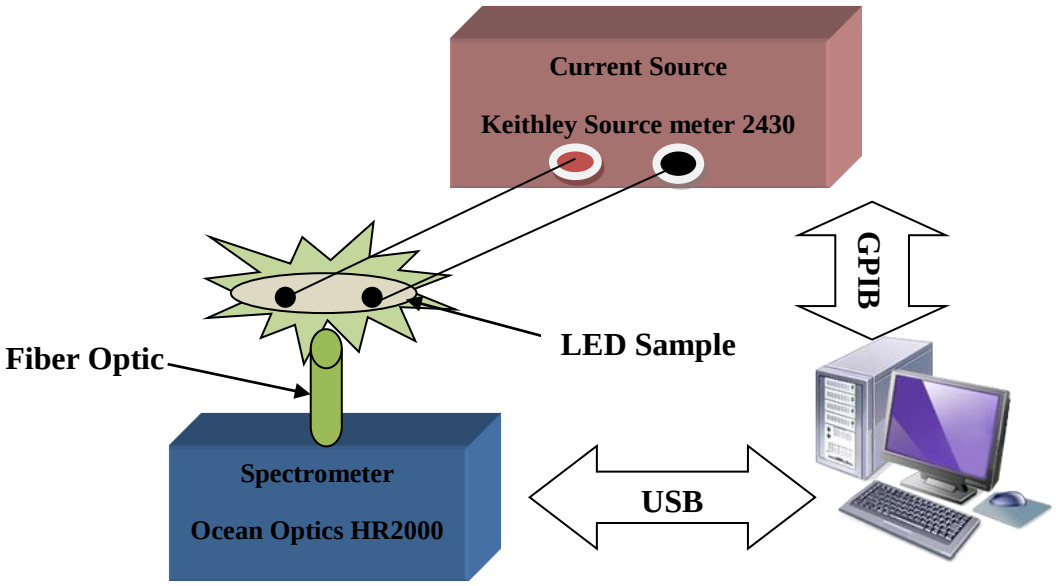

Figure 6.3: Illustration of the EL measurement station

The basic functioning of the EL measurement station is that a current is applied to the LED sample through metallic contacts on the sample surface. Therefore, photons are emitted due to radiative recombination and are transported from the backside of the sample through a fiber optic to the spectrometer. Then, the digital data from the spectrometer is sent to the computer via USB. The program receives and displays the raw data, and saves it to a file along with other useful processed data.

QuickTest 2.0 has a lot of advantages compared to the first version. At first, the execution of the program is faster; it takes seconds instead of minutes to measure a sample. It can control the Keithley source meter and synchronize its execution with the spectrometer,

while these two manipulations had to be done manually previously. The program displays the EL spectrum in real-time and a preview of the overlaid spectrum.

There is no limit of measurements per session compared to nine for the previous version. Finally, the acquisition of the measured Voltages (*I-V* characteristic) is done automatically and saved into the data file instead of writing it down at each measurement.

Therefore, the benefit for the group is a reduction of the measurement time, improvement of repeatability and the results are more accurate due to decrease of heat effect as the measurement process is automatically controlled. Finally, the program is robust and is easily transferable to another computer.

6.3. QuickTest 2.0 front panel and execution

The front panel is the window the user interacts with. It contains the input parameters and displays the EL spectrum, I-V characteristic and processed data result of the LED sample under measurement. The following figure is a screenshot of the front panel.

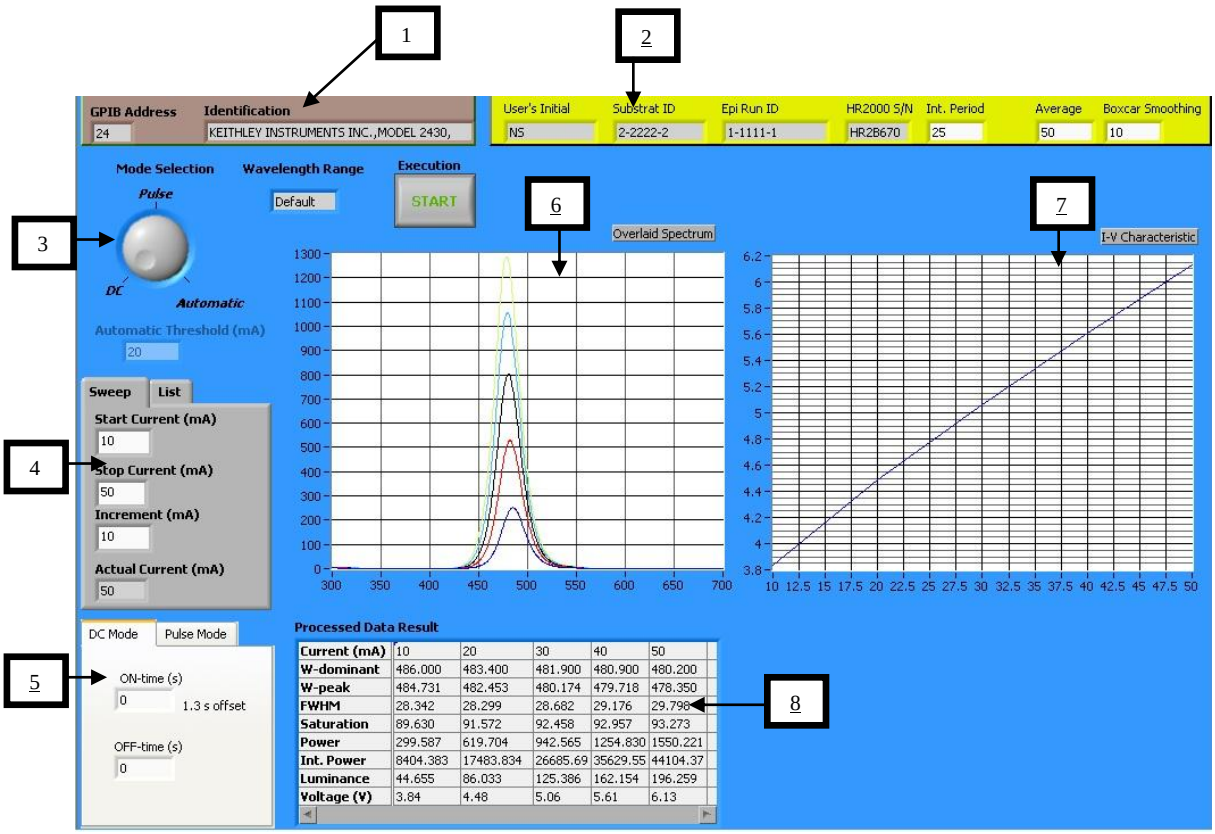

Figure 6.4: Front Panel of QuickTest 2.0

6.3.1. Connection Information Pad

The *GPIB address* is the identification number of the source meter in the GPIB bus. It is required for the program to know which instrument it has to set a communication with. In our setup, 4 different instruments are connected to the computer for different measurement purposes (EL, TLM, oscilloscope and capacitance measurement station). Each instrument has a unique assigned address. The *Identification* string indicator permits to verify that the communication has actually been established.

The program sends an identification request (*IDN?), then the source meter replies back with the following identification string: “KEITHLEY INSTRUMENTS INC., MODEL 2430,”.

6.3.2. Sample information and Spectrometer parameters

The *User’s Initial, Substrate ID and Epi Run ID* are the identification information about the user and the sample under measurement. They are saved in the spectrum and data files’ headers. Concerning *HR2000 S/N*, it is the serial number of the Ocean Optics spectrometer. This information indicates that the spectrometer has been recognized by the computer.

The *Integration Period* specifies the integration time (in ms) of the spectrum acquisition by the spectrometer. It is adjusted so that the anticipated greatest amount of light causes a signal of about 3500 counts.

The *Average* specifies the number of discrete spectral acquisitions that the device driver accumulates before the software receives a spectrum. The higher the value, the better the signal-to-noise ratio (S:N) but the longer the acquisition. The S:N will improve by the square root of the number of scans averaged.

The *Boxcar Smoothing* sets the boxcar smoothing width, a technique that averages across spectral data. This technique averages a group of adjacent detector elements. A value of 5, for example, averages each data point with 5 points to its left and 5 points to its right. The greater this value, the smoother the data and the higher the signal-to-noise ratio.

If the value entered is too high, a loss in spectral resolution will result. The S:N will improve by the square root of the number of pixels averaged.

6.3.3. Mode and Range Selection

Mode Selection selects between DC, Pulse and Automatic modes. When DC is selected, only the DC Mode tab's parameters can be modified and inversely for the Pulse mode. However, when Automatic is selected, both tabs are available for modification.

Automatic mode enables the software to switch between DC and Pulse automatically. The *Automatic Threshold (mA)* control indicates the current threshold from which the switch occurs from DC to Pulse mode. The *Wavelength Range* selects the spectrum saved and displayed: UV (200-400 nm), Blue (350-500 nm), Green (400-600 nm), Default (300 nm to 700 nm) or Full (200 m to 1100 nm) spectrum.

The *Execution* button enables to start the measurement.

6.3.4. Sweep Current/ List Current Control Tabs

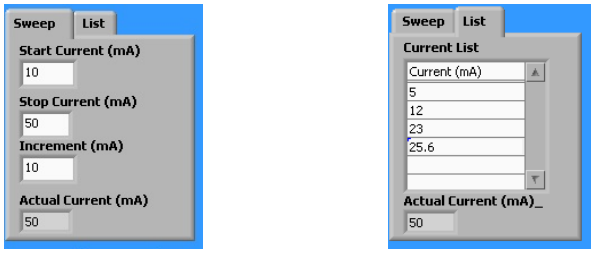

Figure 6.5: (left) Sweep Current Tab and (right) List Tab

The *Sweep Current* tab enables to use the source meter in a current sweep mode with a fix increment. The starting current is entered at the *Start Current* control, the ending current at the *Stop Current* and the *Actual Current* indicates the current that is currently outputted during measurement.

Concerning the *List* tab, it gives the possibility to enter manually the current values.

6.3.5. DC/Pulse Mode parameters Tabs

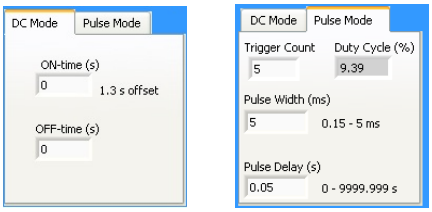

Figure 6.6: (left) DC Mode Tab and (right) Pulse Mode Tab

On *DC Mode*, the *ON-time* is a delay that increases the time during which the source meter output is ON. The minimum is equal to 1.3 s, this lead time is due to the electronics response in the source meter. The *OFF-time* is the time between two measurements when the source meter output is shut off for a very short moment (range of ms). This control allows entering a delay to increase the shut-off time. In *Pulse Mode*, drive current is modulated vs. time using a step function; the pulse configuration is shown in the following figure.

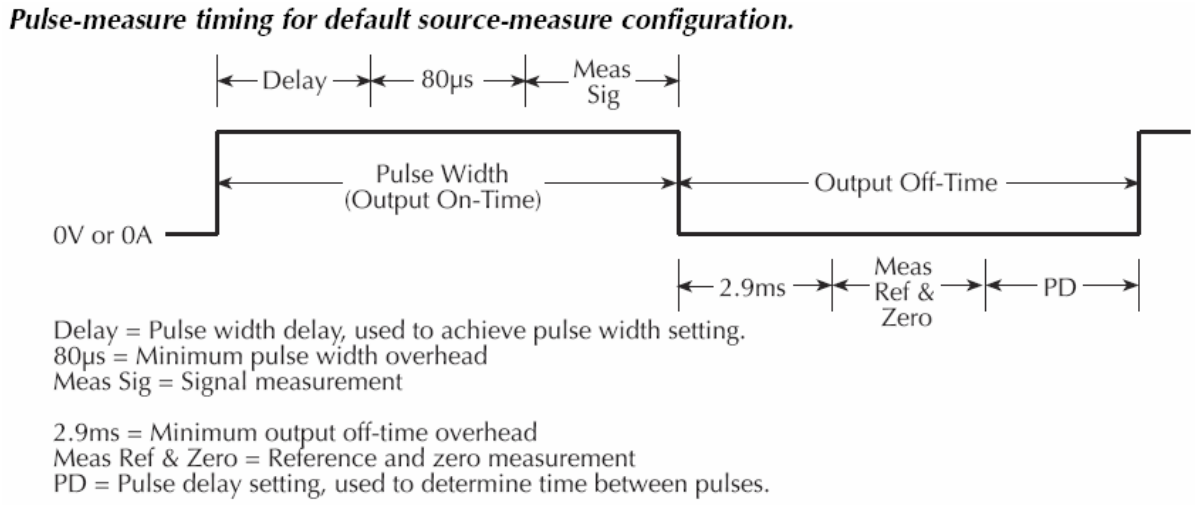

Figure 6.7: Pulse configuration in the source meter (Keithley 2430 User's Manual)

The *Trigger Count* is the number of pulses outputted for each current level. The *Pulse Width* is the width of the pulse (On-Time) that has to be between 0.15 ms and 5 ms. The *Pulse Delay* is the delay during Off-time and has a maximum value of 9999.999 s. The *Duty Cycle* is calculated by the program according to the Pulse Delay and Pulse Width settings.

6.3.6. Spectrum Graphs

This graph displays the spectrum in two steps. A first graph displays the current spectrum under acquisition for each current. At the end, an overlaid spectrum graph shows all plotted spectrum in one graph (as illustrated in the front panel image). The x-axis is automatically sized according to the wavelength range selected. However, the min and max values can be changed at any time and the plot resizes automatically.

6.3.7. I-V Characteristic

It is a graphical display of the I-V result that is updated on real-time for quick assessment of the electrical sample performance.

6.3.8. Processed Data Result

This table summarizes different spectrum characteristic (W=Wavelength, Int.=Integrated): peak wavelength, FWHM, power, voltage, etc. The table size is adjusted automatically according to the number of current values entered.

6.4. Results and comparison

The primarily requirement that the QuickTest 2 software has to meet is that the measurement results from the new program have to be comparable to the previous version. Indeed, the prominent objective of EL measurement is to compare LED samples performance based on arbitrary intensity units (for instance the intensity scale). Therefore, if the light acquisition process differs, there is no possibility to compare recent samples to the previously measured as the arbitrary units changed. The spectrometer requires a lot of different inputs to work, so if one of them is different from the previous version, the result will be different as well.

Thus, the idea was to keep the core of the previous program, which is how the spectrum is acquired by the spectrometer, but change the way it is processed and displayed by the

program along with the programming structures that is responsible for the program execution.

In order to compare the results, a green LED sample has been measured using the two versions of the program at different current levels, from 2 mA to 10 mA (1 mA step) and from 10 mA to 80 mA (10 mA step). The following figures show the variance of intensity at different current levels. The spectrum of interest is from 460 nm to 530 nm.

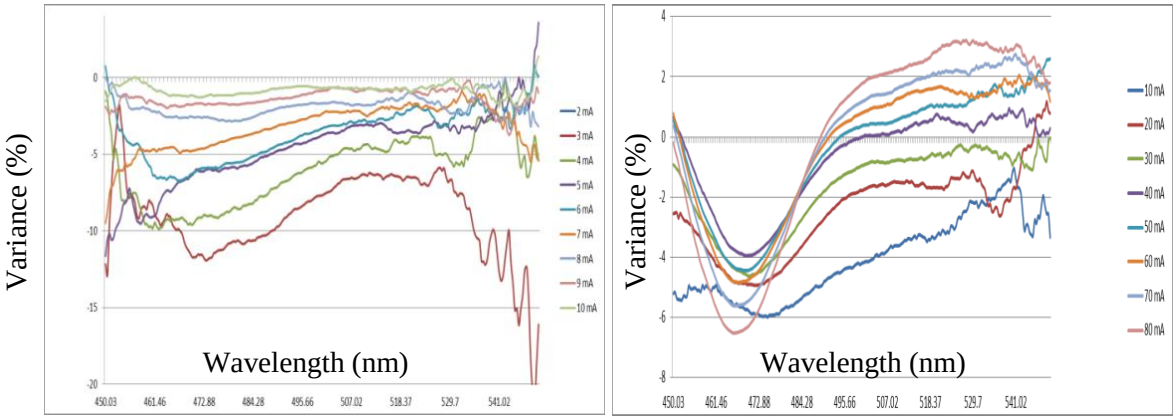

Figure 6.8: Variance of intensity at different currents

In case of low current injection (<10 mA), the difference is inferior or equal to 12 % for the spectrum of interest, and less than 6 % at high current injection (>10 mA). This gap between low and high current injection is due to the fact that at low injection, the intensity is very low and thus a small difference will lead to a higher variance.

However, the most important data used for comparison of samples is the processed data, and more specially the peak wavelength, dominant wavelength and FWHM. The following figure shows the variance for the different processed data.

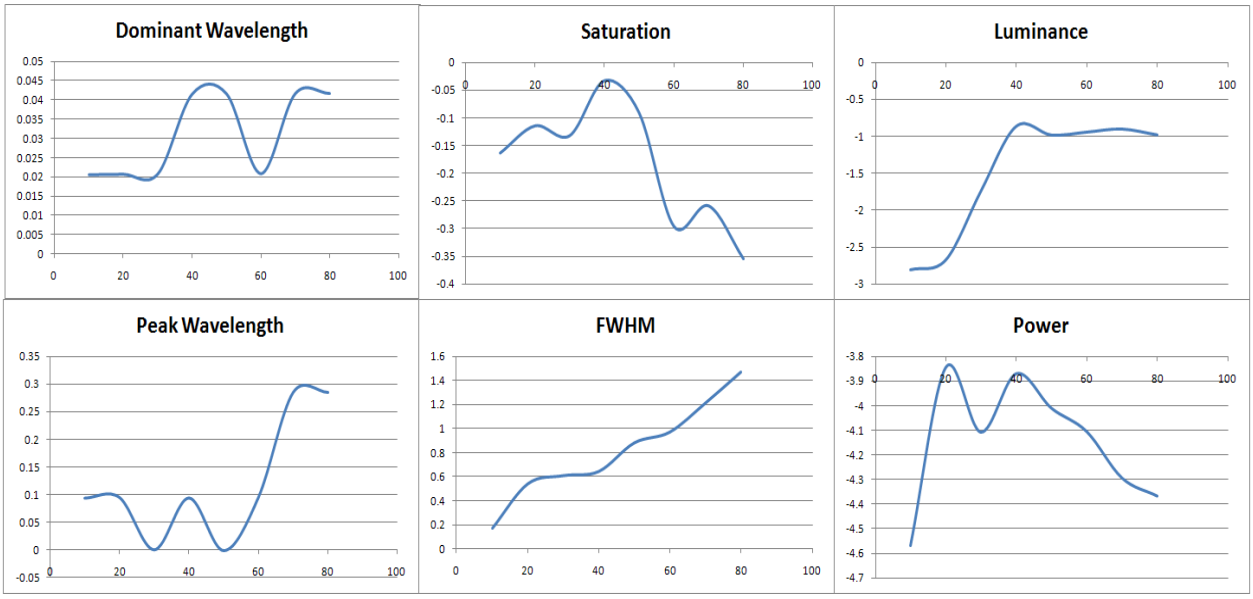

(X-axis = Current (mA) ; Y-axis = Variance (%))

Figure 6.9: Variance of the processed data result at different current levels

As shown on these graphs, the variance for the peak wavelength is less than to 0.3 %, 1.5 % for the FWHM, and 0.05 % for the dominant wavelength, which is more than acceptable. The luminance and power are currently not used and not accurately calculated as they require special setup to be measured such as integrated sphere, but they are still of interest for comparison purpose only.

The variance is pretty high compared to other data because they are directly related to intensity, but lower than 3 % for the luminance and 4.6 % for the power.

Concerning the saturation, this is an indicator of how close the light intensity is to the CCD detector saturation. Its variance is inferior to 0.4 %.

The difference that we experience with QuickTest 2.0 doesn't come from the program itself as the core is the same, but from the way of the measurement is done. Previously, the control of the current source meter and the execution of the measurement were done manually, which vary from user to user and even from the same user. Now, all the process is executed automatically which means that no variation is experienced between measurements, and leads to a better accuracy. This explains why differences in intensity and processed data results exist.

Therefore, the comparison between LED samples is now more efficient than previously, which enables the group to get more accurate data.

7. CONCLUSION

The new challenge the world is facing today is to make energy consumption more efficient as the global energy demand is skyrocketing. The LED device is one of the most promising technologies that will enable to start the "smarter planet" revolution by providing an alternative to inefficient incandescence or phosphorescence lighting, not only in term of performance but also of cost. But, before thinking about deploying this technology, we still have to bridge the "green gap" due to the efficiency reduction effects, by understanding the mechanisms that prevent high-brightness green LEDs from being fabricated. A description of the main effects suspected to be responsible for the efficiency droop, common to all III-N LEDs, which are Auger recombination effect, current overflow and polarization effect have been provided. III-Nitrides are used for blue and green LEDs as they exhibit a direct bandgap and can emit over the entire visible spectrum. A brief discussion about the proprieties of III-Nitrides was given in order to understand the performance of III-N LEDs along with a description of the MOCVD epitaxial growth technique that is mostly used for GaN-related material growth. The discussion of Mg doping of GaN crystals gave a first understanding of the problems related to the p-type layer growth, and introduced the advantage of growing a p-InGaN layer due to a lower growth temperature required but exhibits a higher lattice-mismatch with the active region than p-GaN layer. The issues with LED structure growth and the solutions the group is investigated are discussed in the LED device basics chapter where the characteristics of the n-type, p-type and active region are presented, along with the

device fabrication process. Hole transport is currently under intense investigation as it may be one of the major reasons for efficiency droop. Therefore, different samples are growth with p-GaN and p-InGaN layers in order to study the difference in hole transport.

Research on the design of the Electron-Blocking Layer using InAlN instead of AlGaN resulted in the observation of increase of light intensity by comparing Electroluminescence measurement results of LED structures with EBL made of InAlN versus AlGaN and no EBL.

Device fabrication is of prime importance too on the effort of improving light emission by reducing the metal contact resistance on the p-type layer side, leading to a better hole injection. This has been done by decreasing the Nickel layer thickness from previously 5 nm to 2 nm. Changing the annealing temperature from currently 500^{o}C to 550^{o}C may permit to further decrease contact resistance.

The setup of a Temperature-Dependent Photoluminescence test station enables us to gather important data about the quality of the active region by assessing the internal quantum efficiency. The first set of data shows an IQE of 50% for peak wavelengths of around 490 nm and roughly 35 % for 525 nm, confirming the degradation of LED performance when approaching green wavelengths. In the literature, the highest IQEs published for blue LEDs (450 nm) is around 70 % [47], around 50 % for 490 nm [48] and 40 % for green wavelengths (530 nm) [48]. The data for blue LEDs has been published in 2007 and the green one in 2009.

Finally, a new LabVIEW© program has been developed for EL measurement station. The motivation was to automate the entire station in order to drastically decrease measurement time and to obtain more accurate results thanks to a better repeatability.

REFERENCES

[1] M. R. Krames, O. B. Shchekin, R. Mueller-Mach, G. Mueller, L. Zhou, G. Harbers, and M. G. Craford, "Status and Future of High-Power Light-Emitting Diodes for Solid-State Lighting," *Journal Display Technology*, vol. 3, pp. 160-175, 2007.

[2] J. Hecht, "Photonic Frontiers: Silicon Photonics - Closing in on Silicon Lasers," *Laser Focus World*, Feb. 2006.

[3] C. L. Progl, "High Resolution Electron Beam Testing of Gallium Nitride Based Light Emitting Diodes," Doctoral Dissertation, *North Carolina State University*, 2008.

[4] "Application-Oriented Quantum Theory for Infrared Nitride Lasers? ", *Semiconductor Today*, February 2010.

[5] Z. Lochner, "Green Light Emitting Diodes And Laser Diodes Grown By Metalorganic Chemical Vapor Deposition," Master Thesis, *Georgia Tech*, May 2010.

[6] H. M. Manasevit, "Single-Crystal Gallium Arsenide on Insulating Substrates", *Appl. Phys. Lett.*, vol. 12, pp. 156-159, 1968.

[7] R. D. Dupuis, P. D. Dapkus, R. D. Yingling, and L. A. Moudy, "High-Efficiency GaAlAs/GaAs Heterostructure Solar Cells Grown by Metalorganic Chemical Vapor Deposition", *Appl. Phys. Lett*., vol. 31, pp. 201-203, 1977.

[8] R. D. Dupuis, P. D. Dapkus, J. N. Holonyak, E. A. Rezek, and R. Chin, "Room-Temperature Laser Operation of Quantum-Well $Ga_{(1-x)}Al_xAs$-GaAs Laser Diodes Grown by Metalorganic Chemical Vapor Deposition", *Appl. Phys. Lett*., vol. 32, pp. 295-297, 1978.

[9] D. Yoo, "Growth And Characterization of III-Nitrides Materials System For Photonic and Electronic Devices by Metalorganic Chemical Vapor Deposition," Doctoral Dissertation, *Georgia Tech*, Aug. 2007.

[10] A. Khan, K. Balakrishnan, T. Katona, "Ultraviolet Light-Emitting Diodes Based on Group Three Nitrides," *Nature Photonics*, vol. 2, p. 77-84, 2008.

[11] P-N junction, *Wikipedia*, Aug. 2007.

[12] K. Kumakura, T. Makimoto, N. Kobayashi, "Low-Resistance Nonalloyed Ohmic Contact To P-Type Gan Using Strained Ingan Contact Layer," *Appl. Phys. Lett*., vol. 79, no. 13, 2001.

[13] United States Patent US6744799, *freepatentonline.com*, June 2004.

[14] C. H. Wang et al, *Appl. Phys. Lett*., vol. 97, pp. 261103, 2010

[15] B. Monemar, B. E. Sernelius, "Defect Related Issues in The "Current Roll-Off" in InGaN-Based Light Emitting Diodes", *Appl. Phys. Lett*., vol.91, pp. 181103, Oct. 2007.

[16] I. V. Rozhansky, D. A. Zakheim, "Analysis of The Causes of The Decrease in The Electroluminescence Efficiency of AlGaInN Light Emitting Diode Heterostructures at High Pumping Density", *Semiconductors*, vol. 40, no. 7, pp. 839-845, Jul. 2006.

[17] I. V. Rozhansky, D. A. Zakheim, "Analysis of Processes Limiting Quantum Efficiency of AlGaInN LEDs at High Pumping", *Phys. Status Solidi A*, vol. 204, no. 1, pp. 227-230, Jan. 2007.

[18] I. A. Pope, P. M. Smowton, P. Blood, J. D. Thomson, M. J. Kappers, C. J. Humphreys, "Carrier Leakage in InGaN Quantum Well Light Emitting Diodes Emitting at 480 nm", *Appl. Phys. Lett*., vol. 82, no. 17, pp. 2755-2757, Apr. 2003.

[19] M.-H. Kim, M. F. Schubert, Q. Dai, J. K. Kim, E. F. Schubert, J. Piprek, and Y. Park, "Origin of Efficiency Droop in GaN-Based Light-Emitting Diodes", *Appl. Phys. Lett*., vol. 91, pp. 183507/1-3. Oct. 2007.

[20] M. F. Schubert, J. Xu, J. K. Kim, E. F. Schubert, M. H. Kim, S. Yoon, S. M. Lee, C. Sone, T. Sakong, Y. Park, "Polarization-Matched GaInN/AlGaInN Multi-Quantum-Well Light-Emitting Diodes With Reduced Efficiency Droop", *Appl. Phys. Lett*., vol. 93, pp. 041102, Jul. 2008.

[21] Y. C. Shen, G. O. Mueller, S. Watanabe, N. F. Gardner, A. Munkholm, and M. R. Krames, "Auger Recombination in InGaN Measured by Photoluminescence", *Appl. Phys. Lett*., vol. 91, pp. 141101, Oct. 2007.

[22] A. A. Efremov, N. I. Bochkareva, R. I. Gorbunov, D. A. Larinovich, Yu. T. Rebane, D. V. Tarkhin, and Yu. G. Shreter, "Effect of The Joule Heating on The Quantum Efficiency and Choice of Thermal Conditions for High Power Blue InGaN/GaN LEDs", *Semiconductors*, vol. 40, no. 5, pp. 605-610, May 2006.

[23] S. F. Chichibu, A. Uedono, T. Onuma, S. Nakamura, S. Yamaguchi, S. Kamiyama, H. Amano, I. Akasaki, "Origin of Defect-Insensitive Emission Probability in In-Containing (Al,In,Ga)N Alloy Semiconductors", *Nat. Mater.*, vol. 5, no. 10, pp. 810-816, Oct. 2006.

[24] S. F. Chichibu, T. Sota, K. Wada, and S. Nakamura; "Exciton Localization in InGaN Quantum Well Devices", *J. Vac. Sci. Technol. B*, vol.16, no. 4, pp. 2204-2214, Aug. 1998.

[25] A. R. Vasconcellos, R. Luzzi, C. G. Rodrigues, and V. N. Freire; "Hot Phonon Bottleneck in The Photoinjected Plasma in GaN", *Appl. Phys. Lett*., vol. 82, no. 15, pp. 2455-2457, Apr. 2003.

[26] J. H. Ryou, P. D. Yoder, J. Liu, Z. Lochner, S. Choi, H. J. Kim, R. D. Dupuis, "Control of Quantum Confined Stark Effect in InGaN-Based Quantum Wells"; IEEE *Jour. of Sel. Topics in Quant. Elec*., vol. 15, no. 4, Aug 2009.

[27] Cooke, "Solutions Don't Solve Droop Controversy", *Semiconductor Today*, Compounds and Advanced Silicon, vol. 3, issue 9, Nov 2008.

[28] Shen et al., *Appl. Phys. Lett*., vol. 91, 2007.

[29] Ni et al., *Appl. Phys. Lett*., vol. 93, 2008.

[30] U. Ozgur, H. Liu, X. Li, X. Ni, H. Morkoc, "GaN-Based Light Emitting Diode: Efficiency at High Injection Levels", *Proceedings of the IEEE*, 2009.

[31] A. R. Beattie, P. T. Landsberg, "Auger Effect in Semiconductor", *Proc. R. Soc. Lond. A*., vol. 249, 1959.

[32] J. Hader, J. V. Moloney, B. Pasenow, et al., *Appl. Phys. Lett*., vol. 92, 261103, 2008.

[33] E. Kioupakis, P. Rinke, K. T. Delaney, C. G. Van de Walle, "Indirect Auger Recombination as a Cause of Efficiency Droop in Nitride Light-Emitting Diode," *Appl. Phys. Lett*., vol. 98, pp. 161107, 2011.

[34] E. Kioupakis, P. Rinke, A. Schleife, F. Bechstedt, and C. G. Van de Walle, *Phys. Rev. B*, vol. 81, pp. 241201, 2010.

[35] T. Li, A. M. Fischer, Q.Y. Wei, F. A. Ponce, T. Detchprohm, C. Wetzel, "Carrier Localization and Nonradiative Recombination in Yellow Emitting Ingan Quantum Wells," *Appl. Phys. Lett*., vol. 96, pp. 031906, 2010.

[36] A. M. Fischer, K. W. Sun, E. Juday, F. A. Ponce, J.-H. Ryou, H. J Kim, S. Choi, R. D. Dupuis, "Effect of Growth Temperature on the Electron-Blocking Performance of InAlN Layers in Green Emitting Diodes," *Appl. Phys. Express*, vol. 3, pp. 031003, 2010.

[37] Atomic Force Microscopy, *Wikipedia*, 2009.

[38] NPTEL online classes: http://nptel.iitm.ac.in/courses/Webcourse-contents/IIT-Delhi/Semiconductor%20Devices/LMB2A/2d.htm

[39] University of Santa Barbara: Introduction to X-Ray Diffraction http://www.mrl.ucsb.edu/mrl/centralfacilities/xray/xray-basics/index.html

[40] B. Heying, X. H. Wu, S. Keller, Y. Li, D. Kapolnek, B. P. Keller, S. P. DenBaars, and J. S. Speck, "Role of Threading Dislocation Structure on The X-Ray Diffraction Peak Widths in Epitaxial GaN Films," *Appl. Phys. Lett*., vol. 68, pp. 643-645, 1996.

[41] C. Ryang Wie, "High Resolution X-Ray Diffraction Characterization of Semiconductor Structures," *Materials Sci. and Eng*., vol. 13, pp. 1-56, 1994.

[42] Monochromator, *Wikipedia*, 2010.

[43] Y.-H. Cho, G. H. Gainer, A. J. Fischer, J. J. Song, "S-Shaped Temperature-Dependent Emission Shift and Carrier Dynamics in InGaN/GaN Multiple Quantum Wells," *Appl. Phys. Lett*., vol. 73, pp. 1370, 1998.

[44] S. D. Lester, F. A. Ponce, M. G. Craford, D. A. Steigerwald, "High Dislocation Densities in High Efficiency GaN-Based Light-Emitting Diodes," *Appl. Phys. Lett*., vol. 66, pp. 1249, 1995.

[45] F. Haugen, "Introduction to Simulation with Control Design and Simulation Module in LabVIEW 8.6," *Tech Teach*, March 2009.

[46] ME 295 – Connect LabVIEW, *San Diego State University*, 2011.

[47] J.Y. Tsao, M. E. Coltrin, M. H. Crawford, J. A. Simmons, "Solid-State Lighting: An Integrated Human Factors, Technology and Economic Perspective," *Proc. of IEEE*, 2009.

[48] C. Wetzel, T. Detchprohm, "Closing the Green Gap in LED Materials," Future Chips Constellation, *Rensselaer Polytechnic Institute*, 2009.